*Article*

# Single-Particle Radiation Sensitivity of Ultrawide-Bandgap Semiconductors to Terrestrial Atmospheric Neutrons

**Daniela Munteanu * and Jean-Luc Autran**

Univ Rennes, CNRS, IPR (UMR 6251), 35042 Rennes CEDEX, France; jean-luc.autran@univ-rennes.fr
* Correspondence: daniela.munteanu@univ-rennes.fr

**Abstract:** Semiconductors characterized by ultrawide bandgaps (UWBGs), exceeding the SiC bandgap of 3.2 eV and the GaN bandgap of 3.4 eV, are currently under focus for applications in high-power and radio-frequency (RF) electronics, as well as in deep-ultraviolet optoelectronics and extreme environmental conditions. These semiconductors offer numerous advantages, such as a high breakdown field, exceptional thermal stability, and minimized power losses. This study used numerical simulation to investigate, at the material level, the single-particle radiation response of various UWBG semiconductors, such as aluminum gallium nitride alloys ($Al_xGa_{1-x}N$), diamond, and β-phase gallium oxide (β-$Ga_2O_3$), when exposed to ground-level neutrons. Through comprehensive Geant4 simulations covering the entire spectrum of atmospheric neutrons at sea level, this study provides an accurate comparison of the neutron radiation responses of these UWBG semiconductors focusing on the interaction processes, the number and nature of secondary ionizing products, their energy distributions, and the production of electron–hole pairs at the origin of single-event effects (SEEs) in microelectronics devices.

**Keywords:** atmospheric neutrons; neutron–semiconductor interactions; ultrawide-bandgap semiconductors; aluminum gallium nitride alloys; diamond; gallium oxide; nuclear reactions; Geant4; numerical simulations; single-event effects

Academic Editor: Ludmila Isaenko

Received: 30 January 2025
Revised: 11 February 2025
Accepted: 13 February 2025
Published: 15 February 2025

**Citation:** Munteanu, D.; Autran, J.-L. Single-Particle Radiation Sensitivity of Ultrawide-Bandgap Semiconductors to Terrestrial Atmospheric Neutrons. *Crystals* **2025**, *15*, 186. https://doi.org/10.3390/cryst15020186

**Copyright:** © 2025 by the authors. Licensee MDPI, Basel, Switzerland. This article is an open access article distributed under the terms and conditions of the Creative Commons Attribution (CC BY) license (https://creativecommons.org/licenses/by/4.0/).

## 1. Introduction

Ultrawide-bandgap (UWBG) semiconductors are materials characterized by an exceptionally wide bandgap, far exceeding that of conventional semiconductors such as silicon (1.1 eV), but also typically larger than that of wide-bandgap semiconductors such as silicon carbide (3.2 eV) or gallium nitride (3.4 eV) [1–3]. This offers the advantage of tolerating high fields, since the electric field of avalanche breakdown increases super-linearly with increases in the bandgap energy [1,4,5]. As a result, UWBG semiconductors are particularly well suited for high-power electronics applications such as electric vehicles, motor drives, and power grids, applications that involve high voltages and high power levels [6–11]. Additionally, UWBG semiconductors show high thermal stability, which makes them ideal for use in harsh environments, such as aerospace, automotives, and power systems, where extreme temperatures and radiation may be present [2]. UWBG semiconductors also exhibit high electron mobility [12,13], facilitating fast electron transport. This property is valuable for high-frequency and high-power electronic applications, including radio-frequency (RF) devices [14]. Furthermore, some UWBG semiconductors demonstrate unique optoelectronic properties, such as high transparency in the ultraviolet (UV) region, making them suitable for UV optoelectronic devices, sensors, and detectors [1,8,15,16]. Beyond these applications, UWBG semiconductors are valued for their potential to improve energy efficiency in

electronic devices, reducing power losses and enhancing overall performance. They also play a role in emerging technologies, such as advanced sensors, quantum computing, and next-generation electronic devices [17].

In terms of single-particle radiation sensitivity, UWBG semiconductors are expected to have superior radiation hardness because radiation tolerance scales nonlinearly with the bandgap of the materials [2]. UWBG semiconductors also exhibit a stronger tolerance to cumulative neutron-induced displacement effects due to their higher displacement energy thresholds, typically higher than those of silicon or even silicon carbide [18]. This resilience ensures that semiconductor devices made from UWBG materials can withstand harsh radiation conditions without significant degradation in performance [2,19]. For electronic systems used in space, in nuclear power plants, and in other environments where exposure to radiation is a concern, radiation tolerance both to single-particle effects and cumulated displacement effects is of critical importance. Despite the advantages of UWBG semiconductors for applications in radiation environments, there is little literature addressing the effects of single-particle radiation (i.e., single events) on UWBG materials and devices in contrast to a significant number of publications focusing on cumulative (i.e., many particles) displacement effects. This is primarily due to the difficulties associated with the quality of the materials and the fabrication techniques [17]. Most of these studies are devoted to the effects of radiation on UWBG semiconductor-based devices [19–22], and few studies in the domain of single events have been conducted at the material level. However, the way a material reacts to radiation provides important information about how devices made from that material will respond [23], since these calculations provide a first estimate of the radiation behavior of future devices and circuits that are not yet available or technologically mature enough for real-world testing. The purpose of this paper is then to study the response to single-particle radiation of aluminum gallium nitride alloys ($Al_xGa_{1-x}N$), diamond, and β-phase gallium oxide (β-$Ga_2O_3$) exposed to the natural background of atmospheric neutrons at sea level. This study focuses on the primary neutron interactions with the target material that produce ionizing secondary particles at the origin of single events in components and circuits (these single events occur almost simultaneously with the interaction of neutrons in the material). It does not cover the issue of the cumulative effects of these interactions, which can cause displacement effects (these effects only occur after a certain exposure time required to obtain cumulated doses of at least typically $10^{11}$ n/cm$^2$) [24]. These three semiconductors are among the most widely studied UWBG materials because they can be reliably doped, substrates are available for thin-film growth [1], and devices have been successfully demonstrated [7,25–30]. Only a few studies [31–33] have explored the effects of neutron irradiation on diamond and β-$Ga_2O_3$ at the material level (i.e., without integration into electronic devices). To the best of our knowledge, no published research exists on the sensitivity of $Al_xGa_{1-x}N$ materials to neutron irradiation. In the present paper, we investigate and compare the single-particle radiation response of pure $Al_xGa_{1-x}N$, diamond, and β-$Ga_2O_3$ materials (intrinsic, i.e., undoped, semiconductors) to cosmic ray-induced neutrons produced in the atmosphere at sea level. Previous results on diamond suffer from several limitations regarding the energy of the incident neutrons and the energy of the secondary particles resulting from neutron–diamond interactions. In fact, only the high-energy neutron part of the neutron spectrum was considered in [31], and the study in [33] included only monoenergetic incoming neutrons of 2.45 and 14 MeV from deuterium–deuterium and deuterium–tritium fusion reactions. In addition, a low energy threshold was used in [31], which limited the energy of the secondary particles included in the particle count and analysis. Finally, a small number of incident neutrons was simulated in [31], which could affect the event statistics and simulation results. The limitations of previous studies are overcome in the present work,

since (i) we considered the full spectrum of neutrons at sea level, with neutron energies ranging from thermal to GeV; (ii) we simulated a virtual irradiation of a very large number of incident neutrons ($1.09 \times 10^9$ neutrons, equivalent to $2.5 \times 10^7$ h of exposure in the natural radiation field at sea level from thermal to high-energy neutrons); (iii) no constraint (i.e., filtering) was considered for the energy of the secondary products. The Monte Carlo radiation transport code Geant4 [34–36] was considered to perform the simulation. This code was used to create a dedicated atmospheric neutron source and to construct large databases containing exhaustive information on tens of thousands of neutron interactions with each of the UWBG semiconductors under study. The number and type of interactions (elastic and inelastic scattering and nuclear reactions) along with the number and type of secondary products (protons, alpha particles, fragments) produced in these reactions were quantified and analyzed to compare the atmospheric neutron susceptibilities of $Al_xGa_{1-x}N$, diamond, and $\beta$-$Ga_2O_3$ semiconductors.

The paper is organized as follows: Section 2 presents an overview of the bulk properties of $Al_xGa_{1-x}N$, diamond, and $\beta$-$Ga_2O_3$ materials, as well as the full spectrum of atmospheric neutrons at sea level employed as the source of neutrons in the simulation. This is followed by a detailed explanation of the Monte Carlo numerical simulation of neutron–target interactions using Geant4. Section 3 presents in detail the results of these numerical simulations, focusing on the number and type of interactions, and also on the number and nature of the generated secondary products. This section also includes a comprehensive analysis concerning the distribution in energy of secondary products for each of the three parts of the spectrum of atmospheric neutrons (thermal and low-energy, intermediate-energy, and high-energy neutrons). Finally, Section 4 includes a complete discussion of all the results, with a special focus on the responses of $Al_xGa_{1-x}N$, diamond, and $\beta$-$Ga_2O_3$ materials to atmospheric neutrons, particularly concerning the number of interactions that could potentially trigger substantial single-event effects (SEEs) in devices or circuits.

## 2. Materials and Methods

### 2.1. Material Properties

The density and bandgap energy of the materials studied in this work are presented in Figure 1 and Table 1 [31,37–39]. $Al_xGa_{1-x}N$ is a ternary alloy and its density is calculated using Vergard's law [37,40], which describes the linear dependence of the lattice parameters with the Al content, $x$ ($0 \leq x \leq 1$). The values of the Al content $x$ considered in this work are: 0 (GaN), 0.2, 0.4, 0.6, 0.8, and 1 (AlN). Figure 1 shows the variation in the density of $Al_xGa_{1-x}N$ as a function of $x$, with $x$ varying from 0 to 1. The values for $x = 0$ (GaN) and $x = 1$ (AlN) are also included in Table 1.

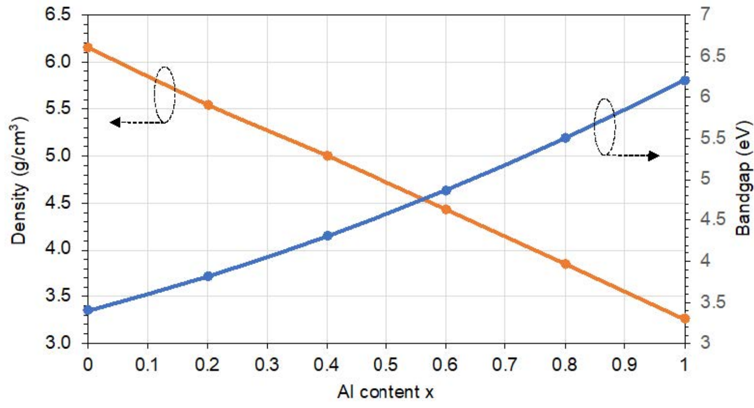


**Figure 1.** Density and bandgap of the ternary alloy $Al_xGa_{1-x}N$ as a function of the Al content $x$.

**Table 1.** Main properties of AlN, GaN, diamond, and β-$Ga_2O_3$ at 300 K.

| Semiconductor | Bandgap @ 300 K $E_g$ (eV) | Density (g/cm$^3$) | Number of Atoms per cm$^3$ | Electron–Hole Pair Creation Energy $E_{eh}$ (eV) |
|---|---|---|---|---|
| AlN | 6.2 | 3.26 | $9.579 \times 10^{22}$ | 15 |
| GaN | 3.4 | 6.15 | $8.85 \times 10^{22}$ | 8.9 |
| C (diamond) | 5.47 | 3.515 | $1.762 \times 10^{23}$ | 13.4 |
| β-$Ga_2O_3$ | 4.6–4.9 | 5.96 | $8.374 \times 10^{22}$ | 15.6 |

It has been experimentally demonstrated that the bandgap energy of ternary alloys such as $Al_xGa_{1-x}N$ follows a quadratic interpolation of the bandgaps of the corresponding binary compounds [41,42]. In the case of an $Al_xGa_{1-x}N$ alloy, the binary compounds are AlN and GaN and its bandgap is given by the equation proposed by [43]:

$$E_g^{Al_xGa_{1-x}N} = xE_g^{AlN} + (1-x)E_g^{GaN} - x(1-x)b \quad (1)$$

In this model, $E_g^{AlN}$ is the bandgap energy of GaN, $E_g^{AlN}$ is the bandgap energy of AlN, and $b$ is a bowing parameter that accounts for deviations from linear interpolation between the two binary compounds. For $Al_xGa_{1-x}N$, the bowing parameter has been reported to be between 0.8 and 1.3 eV [42–45]. The bandgap energy of $Al_xGa_{1-x}N$ as a function of the Al content $x$, as given by Equation (1), is shown in Figure 1. The bandgap of $Al_xGa_{1-x}N$ increases with the Al content $x$ from 3.4 eV (GaN) to 6.2 eV (AlN).

Another important parameter in this study for the analysis of the material sensitivity to neutrons is the mean energy required to create electron–hole pairs, $E_{eh}$. As will be explained later in Section 4, $E_{eh}$ is used to evaluate the conversion of the energy deposited by an ionizing particle into free charge in a given target material. The mean energy for electron–hole pair creation is a material-specific constant typically obtained from experimental measurements or determined from band structure and quantum transport simulations. Klein's phenomenological model, which suggests a linear relationship between the bandgap energy and $E_{eh}$ in semiconductor materials [46], can be used to approximate $E_{eh}$ when experimental or accurate simulated values are not available for a particular semiconductor material. The mean energy for the creation of an electron–hole pair is indicated in Table 1 for AlN, GaN, diamond, and β-$Ga_2O_3$.

Table 2 gives the natural isotopic configuration of the atoms that compose the materials studied in this work: carbon, nitrogen, oxygen, aluminum, and gallium. The natural abundance of each isotope is also included in this table. Aluminum (Z = 13) has one isotope; carbon (Z = 6), nitrogen (Z = 7), and gallium (Z = 31) have two isotopes; and oxygen (Z = 8) has three isotopes.

**Table 2.** Natural abundance of C, N, O, Al, and Ga isotopes considered in this paper.

| Symbol | Atomic Number | Nuclide | Natural Abundance |
|---|---|---|---|
| C | 6 | 6-C-12<br>6-C-13 | 98.93%<br>1.07% |
| N | 7 | 7-N-14<br>7-N-15 | 99.6%<br>0.4% |
| O | 8 | 8-O-16<br>8-O-17<br>8-O-18 | 97.76%<br>0.04%<br>0.20% |
| Al | 13 | 13-Al-27 | 100% |
| Ga | 31 | 31-Ga-69<br>31-Ga-71 | 60.10%<br>39.90% |

### 2.2. Atmospheric Neutron Source

Atmospheric neutrons at sea level originate from the interactions of primary cosmic rays with air particles in the Earth's upper atmosphere. These interactions create atmospheric showers, producing secondary products (particles) that arrive at sea level [47]. The most numerous secondary particles in atmospheric showers are muons, but neutrons are second. Neutrons represent the most serious threat to ground-based electronics. The main reason is that these particles are not charged, which allows them to penetrate deep into circuit materials where they can interact with atoms, producing charged products such as recoil nuclei or secondary ions. These mechanisms are explained in Sections 2.3 and 3.

In this work, we used the full differential flux of atmospheric neutrons produced by cosmic rays recorded at Yorktown Heights [48,49] as the reference input spectrum. This atmospheric neutron spectrum is shown in Figure 2 and has been introduced into our simulator for simulating the interactions of neutrons with the materials considered in this work. The neutron spectrum is partitioned into three domains depending on the neutron energy (Figure 2). Part I includes energies less than 1 eV and refers to thermal and low-energy neutrons. Part II, for neutron energies in the range 1 eV to 1 MeV, refers to intermediate-energy neutrons. Part III, for energies above 1 MeV, corresponds to high-energy neutrons. The cumulated flux across the entire spectrum is 43.6 neutrons per cm$^2$ per hour at sea level (for medium solar activity, outside) [47]. The percentages of the total neutron flux of the three regions of the spectrum are: 17.4% (7.6 neutrons per cm$^2$ per hour) for part I, 36.7% (16 neutrons per cm$^2$ per hour) for part II, and 45.9% (20 neutrons per cm$^2$ per hour) for part III. These values are indicated in Figure 2.

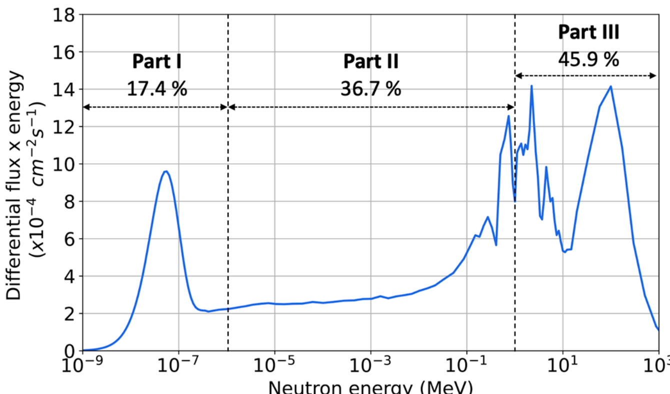


**Figure 2.** Spectrum of the atmospheric neutron (lethargic representation) at sea level recorded on the roof of the IBM Watson Research Center main building [48] in New York City. Experimental data courtesy of Paul Goldhagen (U.S. Department of Homeland Security). Percentages of the total flux of neutrons related to each domain of the spectrum are also indicated.

### 2.3. Neutrons Interaction with Matter

As uncharged particles, neutrons do not undergo Coulomb interactions like charged particles. Neutrons do not interact with orbiting electrons and can then pass across electronic clouds with no interference, i.e., they cannot directly ionize matter. Unlike charged particles, neutrons have very weak electromagnetic interactions. As a result, they have a high degree of penetration and can travel long distances through matter without being obstructed. Neutrons can interact with matter by interacting with atomic nuclei through various mechanisms depending on their energy. Although the probabilities of these interactions are very low, they should not be neglected when studying the radiation sensitivity of electronic materials. This is because these interactions produce secondary charged particles, which can cause single events through the indirect ionization mechanism.

The interactions of neutrons with atomic nuclei are governed by two principal physical mechanisms: scattering and capture. Additionally, scattering mechanisms can be classified as elastic or inelastic [47,50]. In elastic scattering, the particles involved remain unchanged and the recoiling nucleus is identical to the target nucleus. Inelastic scattering is similar but involves an internal rearrangement in the target nucleus, resulting in an excited state and subsequent release of radiation. Beyond scattering, an incoming neutron may be absorbed or captured by the nucleus of the target material. These interactions lead to different possible reactions and the emission of different particles and are collectively known as nuclear reactions (or nonelastic interactions).

A quick way of calculating the total number of interactions occurring between neutrons and a material in a given energy domain is to calculate the reaction rate $R_n$ (number of reactions per second) using [23,51]

$$R_n = N t_{target} \int_{E_{min}}^{E_{max}} \sigma(E) \frac{d\varphi}{dE} dE \quad (2)$$

where $N$ is the number of atoms per $cm^3$ of the material studied (values given in Table 1), $t_{target}$ is the target thickness (expressed in cm), $\sigma(E)$ is the neutron cross-section of the material, $d\varphi/dE$ is the differential neutron flux ($MeV^{-1} \cdot cm^{-2} \cdot s^{-1}$), and $E_{min}$ and $E_{max}$ are the limits of the energy domain taken into account. In this work, we used the neutron cross-sections provided by the TENDL nuclear data library [52] (which includes information about neutron cross-sections up to 200 MeV). The multiplication of $R_n$ by the time period (in seconds) gives the number of reactions for that time period.

### 2.4. Geant4 Simulation Details

We simulated the interactions between atmospheric neutrons and the materials under study following a procedure used in previous studies [31,51]. The simulations were performed using the Monte Carlo radiation transport code Geant4 [32–34], version 4.9.4 patch 01, and taking into account the standard package of physics lists QGSP_BIC_HP [35,36]. More information on the physical processes used for these simulations can be found in [31,32,51].

To simulate the interactions between atmospheric neutrons and materials, pure bulk material targets were subjected to virtual neutron irradiation. Eight materials have been simulated, including six $Al_xGa_{1-x}N$ alloys (with $x$ varying from 0 to 1, by step of 0.2), in addition to diamond and $\beta$-$Ga_2O_3$. We generated one target for each material, where each target had a parallelepiped geometry, with a surface area of 1 $cm^2$ and a thickness of 20 µm, which are the usual dimensions of the sensitive volume of an integrated circuit. Specifically, we chose a thickness of 20 µm because any reaction products that generate an electrical charge beyond this depth would not drift or diffuse into the active zone (i.e., the sensitive region near the surface of the semiconductor). This means that these reaction products would not contribute to creating SEE in the circuit [53]. Each of the eight material targets was exposed to a virtual neutron irradiation with neutrons arriving at normal incidence on the target and an energy distribution corresponding to the spectrum of atmospheric neutrons over the energy parts I, II, and III as described earlier in Section 2.2 (Figure 2). This neutron flux spectrum was introduced into Geant4 via the General Particle Source (GPS) module [54,55] for the random generation of incoming neutrons (perpendicular to the target layer) mimicking this natural neutron background. As explained in the Introduction, a very large number of incoming neutrons is necessary to ensure the accuracy of the simulation results. In this work, for each part of the neutron spectrum, we took into account a number of incident neutrons corresponding to $2.5 \times 10^7$ h of irradiation due to the natural flux of neutrons in the atmosphere at sea level. This exposure time is equivalent

to the following number of primary incident neutrons produced by the Geant4 GPS source: $1.9 \times 10^8$ neutrons for part I of the spectrum, $4 \times 10^8$ neutrons for part II of the spectrum, and $5 \times 10^8$ neutrons for part III of the spectrum.

A Geant4 simulation run generates a database, which is an output file containing extensive details of each neutron interaction with the target material. A total of 24 databases have been generated, one for each of the eight targets and for each of the three domains of the neutron spectrum. Each database contains information such as the type of interaction, the spatial coordinates of the reaction point, and a full list of secondary particles produced. For each emitted particle, the output also includes its energy and emission direction vector. Certain secondary particles, such as positrons, gamma photons, neutral pions, neutrons, or mesons, have a negligeable impact on electronics in terms of electron pair creation and SEEs [56]. For this reason, we have intentionally eliminated these particles, which have weak ionizing characteristics, from the calculated databases. Rare secondary particles, such as charged pions, are also not included in the output file. Thus, the output databases uniquely include lightly charged particles (protons and alpha particles) and other ionizing fragments with an atomic number (Z) superior to 2.

## 3. Results

### *3.1. Number of Interactions*

Figure 3 shows the total number of neutron interactions with the different material targets studied for an equivalent exposure time of $2.5 \times 10^7$ h, obtained from the Geant4 simulations. Neutrons with an energy distribution following the full neutron flux (Figure 2) are considered in this figure. The results show that GaN is the material that produces the highest number of interactions, with diamond in second place, while AlN has the lowest number of interactions. In $Al_xGa_{1-x}N$ materials, the number of interactions is reduced by increasing the percentage $x$ of Al (i.e., reducing the percentage of Ga). β-$Ga_2O_3$ has a lower number of interactions than diamond but a higher number than the $Al_xGa_{1-x}N$ alloys with $x > 0.2$.

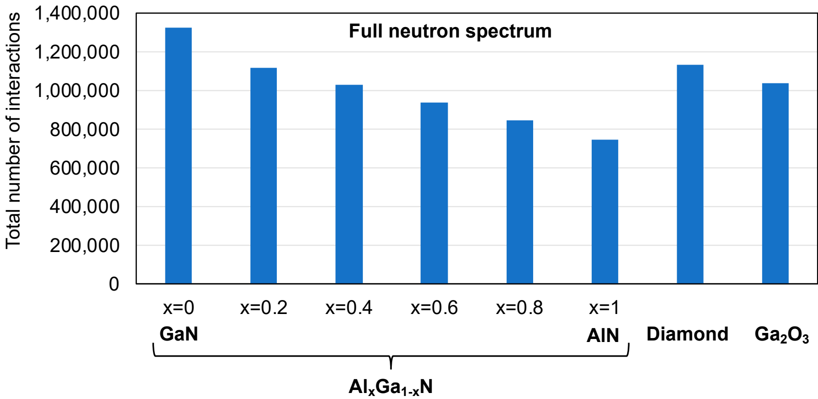


**Figure 3.** Total number of interactions generated by Geant4 simulations of $Al_xGa_{1-x}N$, diamond, and β-$Ga_2O_3$ bulk targets under the full spectrum of atmospheric neutron shown in Figure 2 for an equivalent exposure time of $2.5 \times 10^7$ h.

To go further, we have shown in Figure 4 the respective contributions to the number of interactions from each domain of the neutron spectrum (part I, part II, and part III, as indicated in Figure 2).

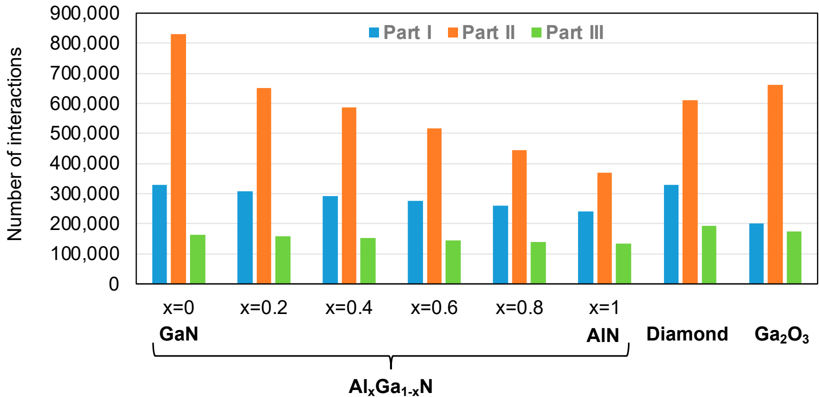


**Figure 4.** Number of neutron interactions in $Al_xGa_{1-x}N$, diamond, and β-$Ga_2O_3$ bulk targets subjected to part I, II, or III of the spectrum of atmospheric neutrons (Figure 2) over $2.5 \times 10^7$ h.

For all materials, part II has the largest contribution to the number of interactions with at least 50% of the total number of interactions (64% for β-$Ga_2O_3$, 50% for AlN, 54% for diamond, and 62% for GaN). Part I has the second largest and part III the smallest contribution to the total number of interactions. To explain this result, we used Equation (2) to quickly calculate the number of neutron interactions with the materials under consideration. According to this formula, the large contribution of part II can be explained by the larger neutron cross-section of the materials for neutrons of intermediate energies and/or by a stronger differential flux in this neutron energy range. For example, for diamond, the neutron cross-section in part II is much larger than in part III, as shown in Figure 5. This figure plots the neutron cross-section of diamond obtained from the TENDL nuclear data open library [52] as a function of neutron energy. For part I, the neutron cross-section is of the same order of magnitude as for part II, but the differential flux is lower, leading to a smaller number of interactions. This is corroborated by the rapid calculation of the number of interactions (from Equation (2)) for each part of the energy range. The results of the calculations for diamond indicate 298,724 interactions for part I, 623,244 interactions for part II, and 182,344 interactions for part III, which are in good agreement with the results of the Geant4 simulations (329,506 interactions for part I, 609,671 interactions for part II, and 193,540 interactions for part III).

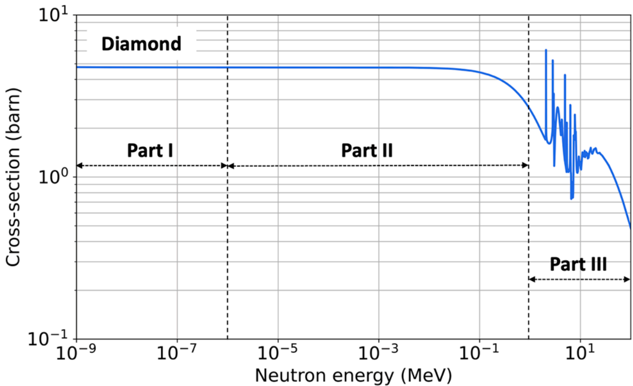


**Figure 5.** Neutron cross-section versus the neutron energy for diamond obtained from the TENDL open nuclear data library.

### 3.2. Type of Interactions

A detailed analysis with respect to the type of interactions is presented in Figure 6, which shows the number of interactions associated with each mechanism, more precisely to elastic and inelastic scattering and to nuclear reactions. This figure indicates that elastic

scattering is the dominant mechanism for all materials, accounting for at least 85% of the total number of interactions. This percentage is as high as 96% for diamond, which is known to be a very effective neutron moderator [57]. The number of nuclear reactions is much lower, below 12% for all materials, and the number of events of inelastic scattering is negligible, below 3%.

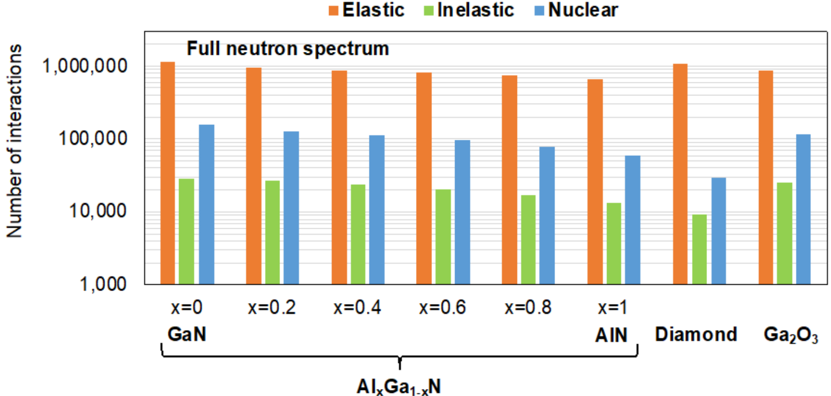


**Figure 6.** Number of events of elastic and inelastic scattering and nuclear reactions in $Al_xGa_{1-x}N$, diamond and β-$Ga_2O_3$ bulk targets under the full spectrum of atmospheric neutrons shown in Figure 2 for an equivalent exposure time of $2.5 \times 10^7$ h.

For $Al_xGa_{1-x}N$ alloys, the numbers of elastic, inelastic, and nuclear interactions decrease as the percentage $x$ of Al increases (i.e., the percentage of Ga decreases). This leads to the results shown previously in Figure 3, where the total number of interactions decreases as $x$ increases. Thus, among the $Al_xGa_{1-x}N$ alloys, AlN has the lowest interaction count for all mechanisms, much lower than GaN. For example, AlN produces 40.6% less elastic scattering than GaN, half as much inelastic scattering, and a 63% reduction in the number of nuclear reactions.

Details of the number of events for each interaction mechanism across all the materials are given in Table 3, Table 4, and Table 5 for domains I, II, and III of the spectrum of atmospheric neutrons, respectively. Analysis of these data shows that for neutrons with thermal and low energies (part I of the spectrum, Table 3), β-$Ga_2O_3$ has the lowest interaction number of all materials, followed by AlN in second place, while diamond and GaN have the highest interaction numbers due to a very high number of events of elastic scattering. Note that for part I of the spectrum, there is no inelastic scattering (as shown in Table 3) because the neutron energy is below the energy threshold required for this mechanism to occur.

**Table 3.** Number of events of elastic and inelastic scattering and nuclear reactions in $Al_xGa_{1-x}N$, diamond, and β-$Ga_2O_3$ bulk targets exposed to part I (neutron energy less than 1 eV) of the spectrum of atmospheric neutrons (Figure 2) for an equivalent exposure time of $2.5 \times 10^7$ h.

| Material | | Elastic | Inelastic | Nuclear |
|---|---|---|---|---|
| $Al_xGa_{1-x}N$ | $x = 0$ (GaN) | 265,632 | 0 | 63,979 |
| | $x = 0.2$ | 251,436 | 0 | 57,013 |
| | $x = 0.4$ | 241,788 | 0 | 50,745 |
| | $x = 0.6$ | 231,333 | 0 | 44,403 |
| | $x = 0.8$ | 222,060 | 0 | 37,934 |
| | $x = 1$ (AlN) | 211,971 | 0 | 30,612 |
| Diamond | | 329,294 | 0 | 212 |
| β-$Ga_2O_3$ | | 166,971 | 0 | 33,365 |

**Table 4.** Number of events of elastic and inelastic scattering and nuclear reactions in $Al_xGa_{1-x}N$, diamond, and β-$Ga_2O_3$ bulk targets subjected to part III (neutron energy between 1 eV and 1 MeV) of the spectrum of atmospheric neutrons (Figure 2) for an equivalent exposure time of 2.5 × $10^7$ h.

| Material | | Elastic | Inelastic | Nuclear |
|---|---|---|---|---|
| $Al_xGa_{1-x}N$ | $x = 0$ (GaN) | 772,115 | 1073 | 57,363 |
| | $x = 0.2$ | 612,536 | 2105 | 35,665 |
| | $x = 0.4$ | 556,444 | 1603 | 27,826 |
| | $x = 0.6$ | 496,213 | 1096 | 19,648 |
| | $x = 0.8$ | 433,700 | 547 | 10,853 |
| | $x = 1$ (AlN) | 368,779 | 29 | 1458 |
| Diamond | | 609,668 | 0 | 3 |
| β-$Ga_2O_3$ | | 612,955 | 951 | 48,649 |

**Table 5.** Number of events of elastic and inelastic scattering and nuclear reactions in $Al_xGa_{1-x}N$, diamond, and β-$Ga_2O_3$ bulk targets subjected to part III (neutron energy higher than 1 MeV) of the spectrum of atmospheric neutrons (Figure 2) for an equivalent exposure time of 2.5 × $10^7$ h.

| Material | | Elastic | Inelastic | Nuclear |
|---|---|---|---|---|
| $Al_xGa_{1-x}N$ | $x = 0$ (GaN) | 99,580 | 26,984 | 38,035 |
| | $x = 0.2$ | 97,357 | 24,579 | 35,306 |
| | $x = 0.4$ | 96,615 | 21,972 | 33,248 |
| | $x = 0.6$ | 95,736 | 19,161 | 31,156 |
| | $x = 0.8$ | 94,702 | 16,246 | 29,236 |
| | $x = 1$ (AlN) | 94,039 | 13,373 | 27,042 |
| Diamond | | 155,705 | 9185 | 28,650 |
| β-$Ga_2O_3$ | | 113,997 | 23,975 | 35,877 |

Table 4 shows that interactions with intermediate-energy neutrons (part II of the spectrum) are the least numerous for AlN, which produces more than half as much elastic scattering as GaN and has a very low number of events of inelastic scattering and nuclear reactions. As for part I of the spectrum, the number of interactions decreases as the Al content $x$ increases in the $Al_xGa_{1-x}N$ alloys. Of all the materials, GaN has the highest number of interactions with neutrons of intermediate energy, which is dominated to a very large extent by elastic scattering. For high-energy neutrons (Table 5), AlN exhibits the lowest number of events of elastic scattering and nuclear reactions, and diamond shows the lowest number of events of inelastic scattering. However, diamond has the highest number of events of elastic scattering for this neutron energy range due to its neutron moderator properties.

### *3.3. Number and Nature of Secondary Products*

All of the above-mentioned interactions between incoming neutrons and target materials produce either a single secondary product or multiple. Figure 7 shows the number of secondary products that result from interactions between neutrons with energies in domains I, II, and III of the spectrum of atmospheric neutrons and $Al_xGa_{1-x}N$, diamond, or β-$Ga_2O_3$ targets. These results show that, for all the materials, the highest number of products is obtained for interactions with neutrons in part II of the spectrum, and the smallest number of products is obtained for interactions with neutrons in part III. Of the materials considered here, GaN produces the highest number of secondary products for parts I and II of the spectrum, and diamond produces the highest number of products for part III. The lowest number of products is obtained for β-$Ga_2O_3$ in part I of the spectrum and for AlN in parts II and III. In addition, Figure 7 shows that for $Al_xGa_{1-x}N$ alloys, the number of secondary products decreases as Al content $x$ increases for all three parts of the spectrum.

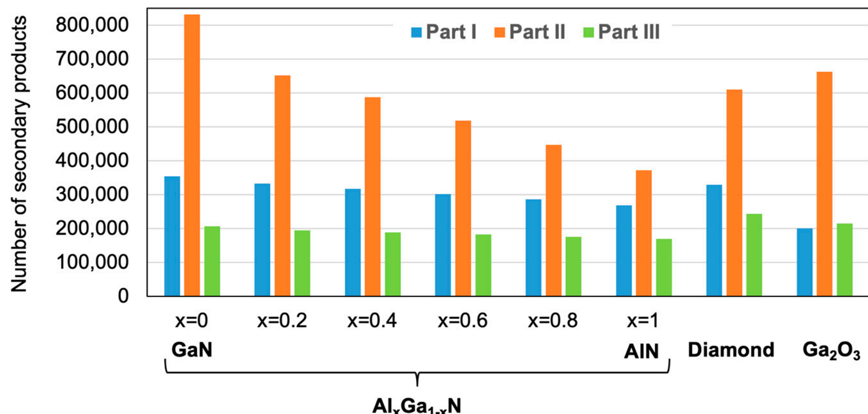


**Figure 7.** Number of secondary products in $Al_xGa_{1-x}N$, diamond, and β-$Ga_2O_3$ bulk targets subjected to part I, II, or III of the spectrum of atmospheric neutrons (Figure 2) over $2.5 \times 10^7$ h.

The total number of secondary products generated during an interaction is referred to as "secondary product shower multiplicity", as each interaction initiates a cascade of ionizing particles. In this work, secondary products with low ionizing properties such as neutrons, gamma photons, electrons, pions, positrons, and mesons were eliminated from the databases (see explanations in Section 2.4). They were then not counted when calculating the shower multiplicity. As such, a multiplicity of 1 signifies the emission of a single ionizing product and is associated with elastic scattering, inelastic scattering, or particular neutron capture event (neutron capture (n,$\gamma$) reactions emitting gamma photons and recoil products, for example, $^{69}$Ga(n,$\gamma$)$^{70}$Ga; see also Section 3.4). In contrast, higher multiplicities indicate that a nuclear reaction is involved, which results in the generation of two or more ionizing secondary products. The number of interactions versus the shower multiplicity for $Al_xGa_{1-x}N$ alloys, diamond, and β-$Ga_2O_3$ targets subjected to the full spectrum of atmospheric neutrons is shown in Figure 8. These results show that for all the materials, the number of interactions that lead to a single product (shower multiplicity of 1) is by far the highest. For all the materials, more than 90% of the total number of interactions have a shower multiplicity of 1. This is consistent with previous results on the number of elastic and inelastic scattering events reported in Figure 6. The number of interactions with a shower multiplicity greater than 1 is much lower, which is again consistent with the number of nuclear reactions reported previously. We also notice that the number of interactions decreases as the shower multiplicity increases, and beyond a certain multiplicity there are no more interactions.

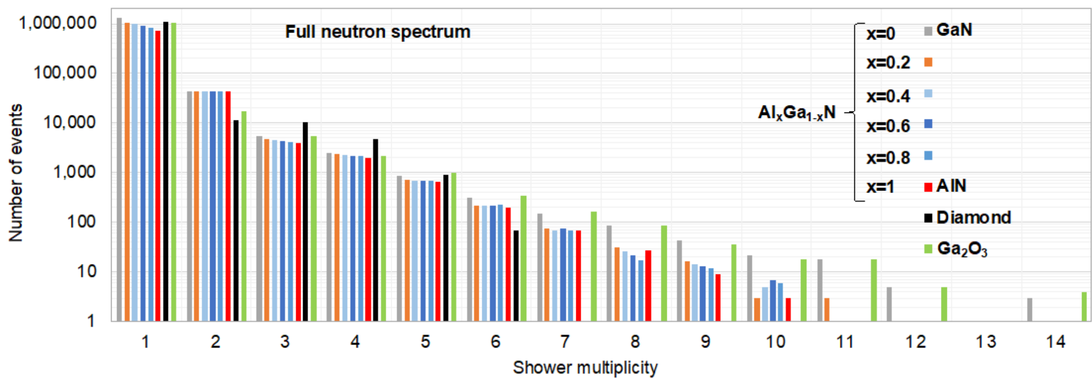


**Figure 8.** Number of events versus the shower multiplicity for $Al_xGa_{1-x}N$, diamond, and β-$Ga_2O_3$ bulk targets subjected to the full spectrum of atmospheric neutrons (Figure 2) over $2.5 \times 10^7$ h.

Looking at reactions that produce multiple fragments, events with a multiplicity of four or more account for less than 0.5% of the occurrences across all materials. Despite their rarity, high-multiplicity events are important because they can produce single events that can affect multiple sensitive regions within a device or a circuit. For shower multiplicities above 11, the statistical relevance of such events is significantly reduced and may be affected by the number of incident neutrons, as discussed in [31].

A detailed analysis of the exact nature of the secondary products is presented in Figure 9, which shows the number of products for each atomic number Z. For the sake of simplicity, only three $Al_xGa_{1-x}N$ alloys, GaN, $Al_{0.6}Ga_{0.4}N$, and AlN, are considered in addition to diamond and β-$Ga_2O_3$. As usual for neutron–matter interactions [58], the range of atomic numbers of the secondary products extends from 1 (proton) to the highest atomic number present in the target material. In this study, the maximum Z values are Z = 6 for diamond, Z = 13 for AlN, and Z = 31 for the other $Al_xGa_{1-x}N$ alloys and for β-$Ga_2O_3$. However, a few nitrogen atoms are produced when diamond interacts with neutrons, as well as a few germanium atoms when gallium-containing materials interact with neutrons. The explanation is that rare transmutation reactions can produce products with higher atomic numbers [23]. In our simulations, which involve a very large number of incident neutrons, this phenomenon is clearly visible (in Figure 9), with some carbon nuclei being transmuted into nitrogen, some aluminum nuclei being transmuted into silicon, and some gallium nuclei being transmuted into germanium (similar results have already been reported in [23]).

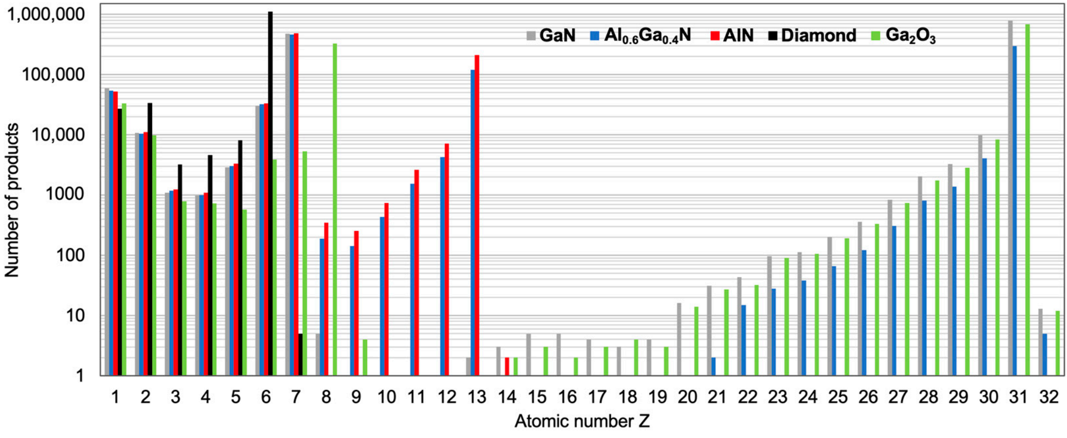


**Figure 9.** Number of secondary products versus the atomic number Z for GaN, $Al_{0.6}Ga_{0.4}N$, AlN, diamond, and β-$Ga_2O_3$ bulk under the full spectrum of atmospheric neutron shown in Figure 2 over $2.5 \times 10^7$ h.

Figure 9 shows that for each of the materials examined in this study, the most commonly produced secondary particles are recoil products generated by the elastic or inelastic scattering of neutrons with the nuclei of the semiconductor target or by neutron capture in (n,$\gamma$) reactions. For compound materials, the recoil nuclei correspond to the different species that compose the material: in the case of AlN, the recoil nuclei are Al and N; for GaN, the recoil nuclei are Ga and N; for all other $Al_xGa_{1-x}N$ alloys, the recoil nuclei are Al, Ga, and N; and in the case of β-$Ga_2O_3$, the recoil nuclei are Ga and O. The second most abundant secondary products are protons for all materials except diamond, where they are alpha particles. For $Al_xGa_{1-x}N$ alloys, carbon (more precisely $^{14}$C nuclei) is the third most abundant secondary product. For diamond, protons are in third place, and for β-$Ga_2O_3$, alpha particles are third. Much smaller quantities of other secondary products are produced.

In the specific case of $Al_xGa_{1-x}N$ alloys, the high concentration of protons and $^{14}C$ is largely due to the interaction of neutrons with nitrogen following the reaction $^{14}N(n,p)^{14}C$. The neutron capture process involving nitrogen nuclei can lead to the generation of secondary particles, which pose a significant challenge to the radiation reliability of materials or devices containing nitrogen. This concern has been addressed in a recent study [59] that demonstrated its impact within silicon technologies using nitride layers. The issue is then particularly relevant to devices based on $Al_xGa_{1-x}N$ alloys. When nitrogen captures neutrons, it produces secondary products such as energetic protons with an energy of 584 keV and $^{14}C$ nuclei with an energy of 42 keV. These secondary products can transfer significant energy to the semiconductor material. Specifically, each 584 keV proton can induce an electrical charge transfer of more than 10 fC, while 42 keV $^{14}C$ nuclei can transfer nearly 0.8 fC. These energy transfers are substantial and can result in large amounts of charge deposited within the material, potentially affecting device performance and reliability under radiation exposure.

A final comment concerns the number of secondary products for each Z. Figure 9 shows that at low Z values (Z between 2 and 6), diamond produces a much larger number of secondary products than any of the other materials investigated here due to its much higher atomic concentration. When Z is between 8 and 13, AlN produces more secondaries than $Al_{0.6}Ga_{0.4}N$, with these secondary products coming from reactions between neutrons and Al atoms, because neutron–Ga interactions do not produce products in this Z range. Since Al has a concentration that is 74.1% higher in AlN than in $Al_{0.6}Ga_{0.4}N$, the number of secondary products is thus higher in AlN than in $Al_{0.6}Ga_{0.4}N$. For $Z > 14$, only the reactions of neutrons with GaN, $Al_{0.6}Ga_{0.4}N$, and $\beta$-$Ga_2O_3$ produce secondary products, which are the result of nuclear reactions between neutrons and Ga atoms. For this Z range, GaN has the highest production of secondary products, as shown in Figure 9. The explanation is that the Ga concentration in GaN is 32% higher than in $Ga_2O_3$ and almost 3.5 times higher than in $Al_{0.6}Ga_{0.4}N$, and therefore, GaN produces more secondary products than $\beta$-$Ga_2O_3$ and especially more than $Al_{0.6}Ga_{0.4}N$.

### *3.4. Energy Distributions of Secondary Products*

A detailed analysis of these secondary products from an energy point of view is presented in this section. Energy histograms for each part of the spectrum and for each material are presented in Figures 10–15. The energy distributions of the secondary products produced in the $Al_xGa_{1-x}N$ alloy targets by the incident thermal and low-energy neutrons (part I of the neutron atmospheric spectrum) are shown in Figure 10a–c. For each material, the secondary products correspond to the nuclei of the atoms of the given material and the protons and $^{14}C$ nuclei resulting from the reaction $^{14}N(n,p)^{14}C$. It should be noted that the secondary products can have much higher energies than the incident neutrons, which have energies of less than 1 eV. This is due to energy release by the nucleus during $(n,\gamma)$ capture or (n,p) nuclear reactions.

Figure 10a–c show two distinct bell-shaped distributions, as well as two mono-energetic distributions corresponding to protons and $^{14}C$ nuclei. The first bell-shaped distribution corresponds to the recoil nuclei resulting from the elastic scattering mechanisms (n,n): Ga and N for GaN in Figure 10a; Al, Ga, and N for $Al_{0.6}Ga_{0.4}N$ in Figure 10b; and Al and N for AlN in Figure 10c. For all the materials, this distribution has a maximum around 0.1 eV. The second bell-shaped distribution corresponds to the neutron capture $(n,\gamma)$ reactions emitting gamma photons and recoil products as shown in Figure 10a–c. For example, for $Al_{0.6}Ga_{0.4}N$, these reactions are as follows: $^{69}Ga(n,\gamma)^{70}Ga$ and $^{71}Ga(n,\gamma)^{72}Ga$ yielding $^{70}Ga$ and $^{72}Ga$ products with energies in the range eV to keV, $^{27}Al(n,\gamma)^{28}Al$ producing a distribution of $^{28}Al$ ranging from tens of eV to tens of keV, and $^{14}N(n,\gamma)^{15}N$ that

produces a distribution of $^{15}N$ in the range hundreds of eV to tens of keV. Finally, for all the $Al_xGa_{1-x}N$ alloys, two mono-energetic distributions at high energy appear, corresponding to $^{14}C$ nuclei of 42 keV and protons of 584 keV, which are secondary products of the reaction $^{14}N(n,p)^{14}C$. As explained above, high-energy $^{14}C$ nuclei and protons are a concern for the radiation reliability of components based on materials containing nitrogen.

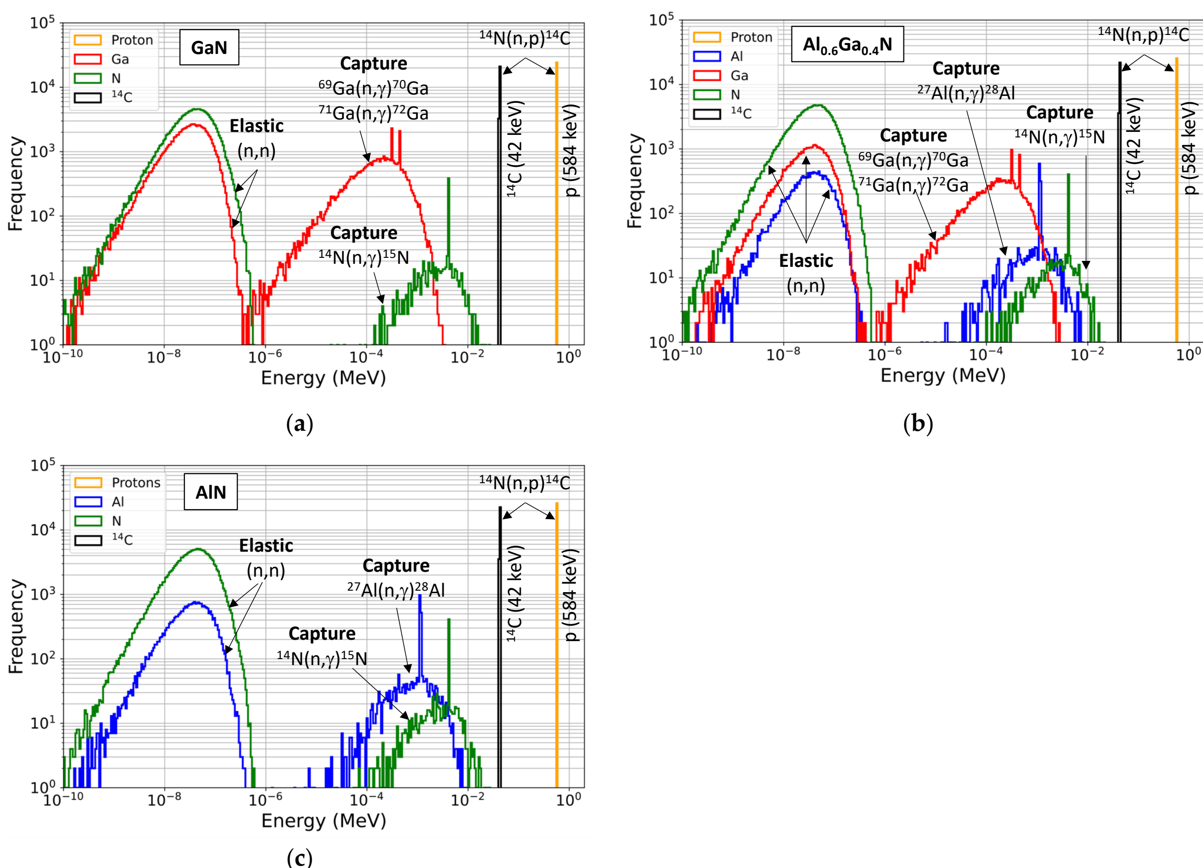


**Figure 10.** Energy histograms (500 bins) of the secondary products generated in the $Al_xGa_{1-x}N$ alloy targets (1 $cm^2$ × 20 μm) irradiated with neutrons of energies less than 1 eV (part I of the spectrum) over 2.5 × $10^7$ h. (**a**) GaN; (**b**) $Al_{0.6}Ga_{0.4}N$; (**c**) AlN.

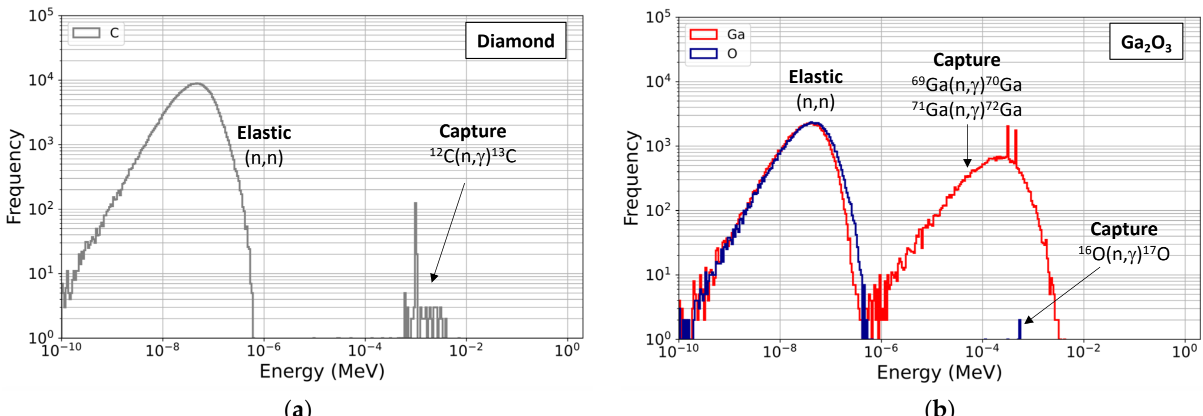


**Figure 11.** Energy histograms (500 bins) of the secondary products generated in the diamond and β-$Ga_2O_3$ targets (1 $cm^2$ × 20 μm) irradiated with neutrons of energies less than 1 eV (part I of the spectrum) over 2.5 × $10^7$ h. (**a**) Diamond; (**b**) β-$Ga_2O_3$.

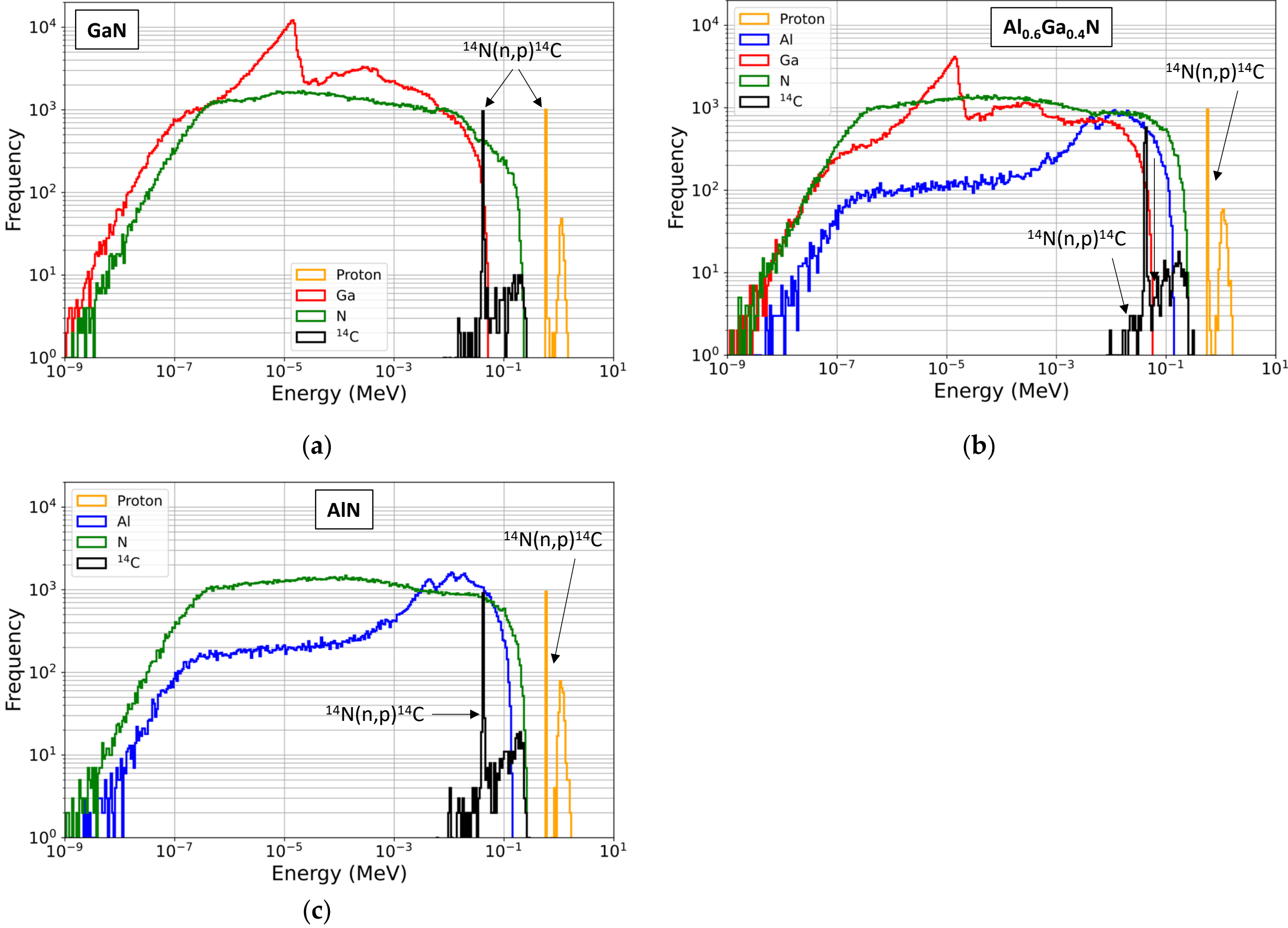


**Figure 12.** Energy histograms (500 bins) of the secondary products generated in the $Al_xGa_{1-x}N$ alloy targets (1 cm$^2$ × 20 μm) irradiated with neutrons of energies between 1 eV and 1 MeV (part II of the spectrum) over 2.5 × 10$^7$ h. (**a**) GaN; (**b**) $Al_{0.6}Ga_{0.4}N$; (**c**) AlN.

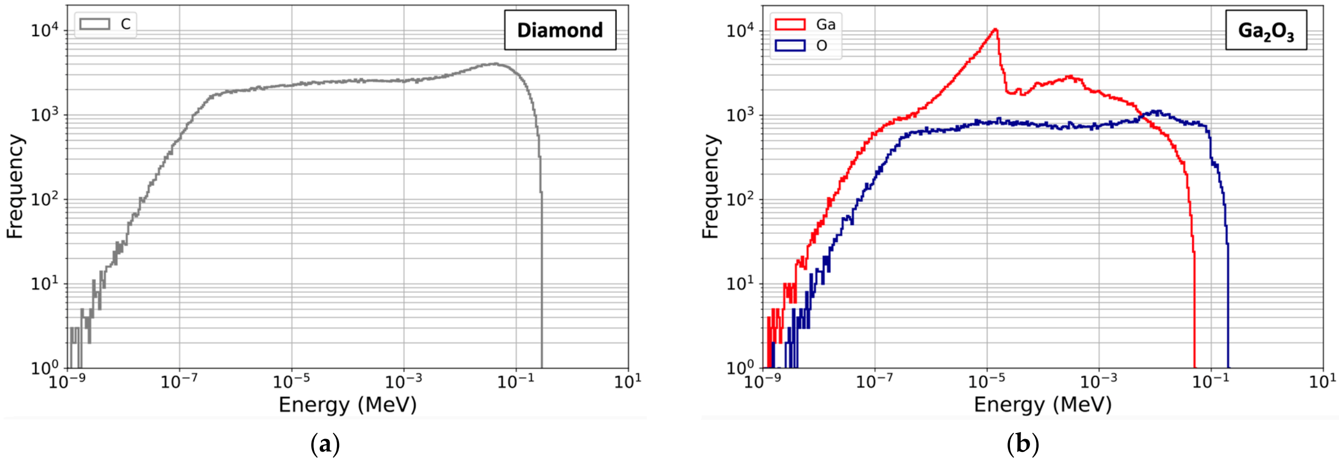


**Figure 13.** Energy histograms (500 bins) of the secondary products generated in the diamond and β-$Ga_2O_3$ targets (1 cm$^2$ × 20 μm) irradiated with neutrons of energies between 1 eV and 1 MeV (part II of the spectrum) over 2.5 × 10$^7$ h. (**a**) Diamond; (**b**) β-$Ga_2O_3$.

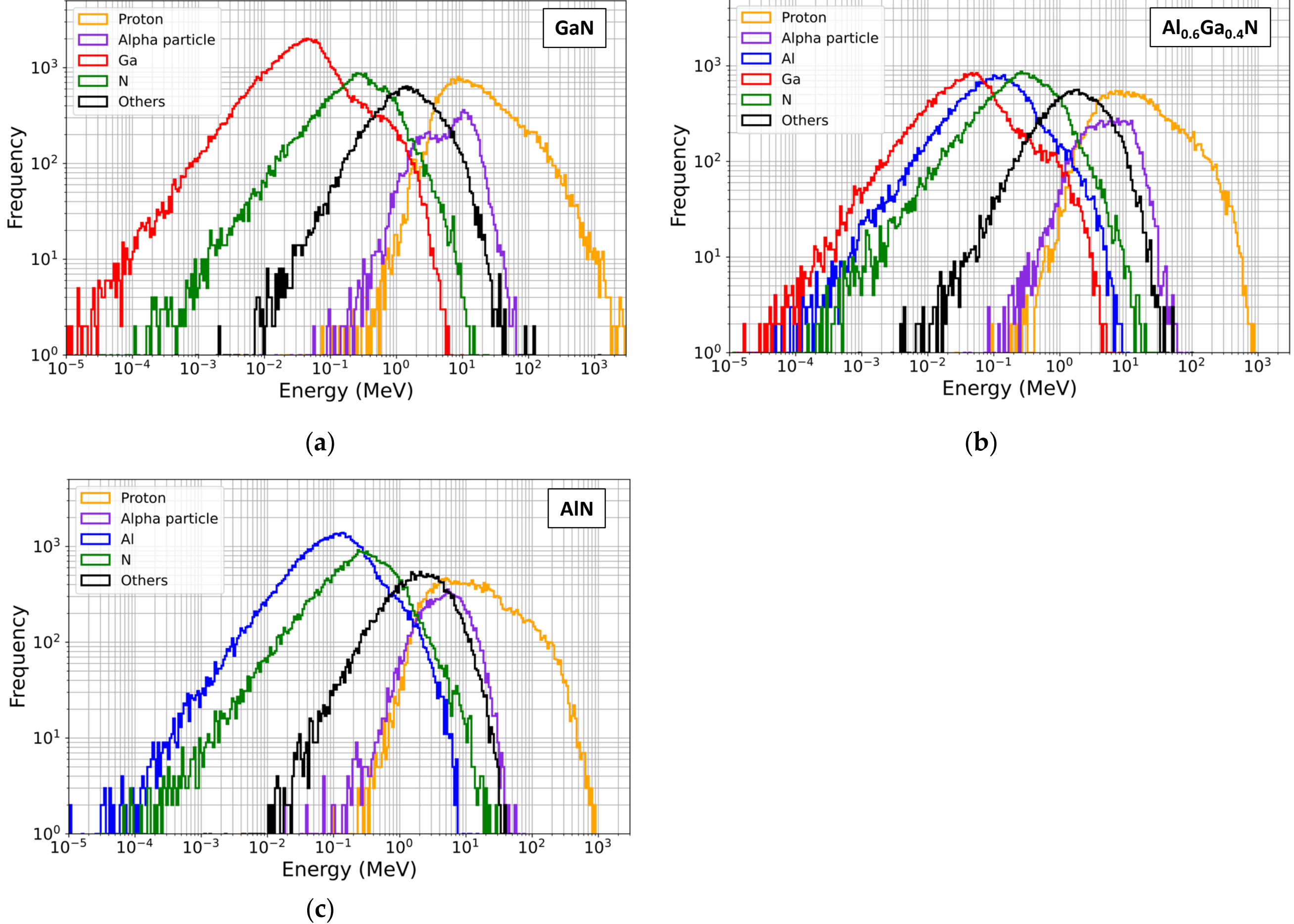


**Figure 14.** Energy histograms (500 bins) of the secondary products generated in the $Al_xGa_{1-x}N$ alloy targets (1 $cm^2$ $\times$ 20 µm) irradiated with neutrons of energies higher than 1 MeV (part III of the spectrum) over 2.5 $\times$ $10^7$ h. (**a**) GaN; (**b**) $Al_{0.6}Ga_{0.4}N$; (**c**) AlN.

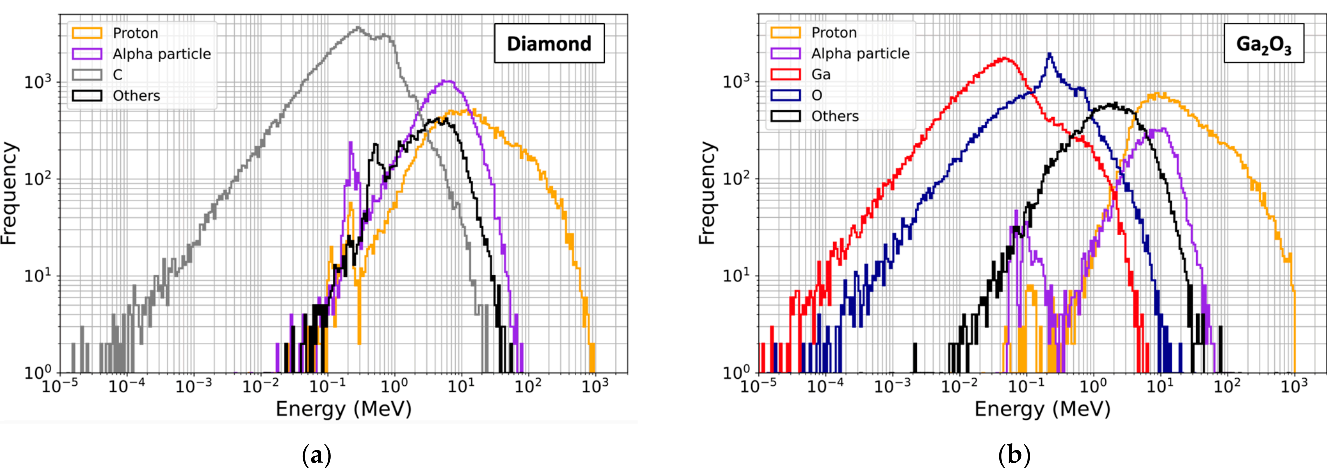


**Figure 15.** Energy histograms (500 bins) of the secondary products generated in the diamond and β-$Ga_2O_3$ targets (1 $cm^2$ $\times$ 20 µm) irradiated with neutrons of energies higher than 1 MeV (part III of the spectrum) over 2.5 $\times$ $10^7$ h. (**a**) Diamond; (**b**) β-$Ga_2O_3$.

Figure 11a,b show the energy histograms of the secondary products resulting from interactions of thermal and low-energy incident neutrons (part I of the atmospheric neutron spectrum) with diamond and β-$Ga_2O_3$. As in the case of $Al_xGa_{1-x}N$ alloys, the recoil nuclei produced during elastic scattering (C for diamond, Ga and O for β-$Ga_2O_3$) show

a bell-shaped energy distribution with a maximum around 0.1 eV. The energies of these recoil nuclei are less than 1 eV. Secondary products with higher energies than the incident neutrons are the result of the following capture reactions: rare $^{12}C(n,\gamma)^{13}C$ reactions for diamond and $^{71}Ga(n,\gamma)^{72}Ga$, $^{69}Ga(n,\gamma)^{70}Ga$, and $^{16}O(n,\gamma)^{17}O$ reactions for β-$Ga_2O_3$. In diamond, the capture reaction $^{12}C(n,\gamma)^{13}C$ has a much lower frequency than the elastic scattering reactions. This is also the case for the $^{16}O(n,\gamma)^{17}O$ reaction, which occurs only a few times. The products of the $^{71}Ga(n,\gamma)^{72}Ga$ and $^{69}Ga(n,\gamma)^{70}Ga$ capture reactions have a bell-shaped energy distribution with a peak around 0.2 keV. For both materials, the maximum energy of the secondary products is around 4 keV.

Figures 12 and 13 show the energy histograms of the secondary products resulting from the interactions of intermediate-energy neutrons (part II of the atmospheric neutron spectrum) with the target materials. Elastic scattering (n,n) between neutrons and the nuclei of the materials accounts for the vast majority of secondary products (over 92% for all materials; see also Table 4). As for part I of the spectrum, for all the materials, the secondary products are exclusively nuclei of the atoms that constitute the material; for $Al_xGa_{1-x}N$ alloys, there is an additional contribution of $^{14}C$ nuclei and protons from the $^{14}N(n,p)^{14}C$ reaction. This reaction channel is always open, but the quantities of $^{14}C$ nuclei and protons produced are smaller than those resulting from interactions with neutrons that have energies in part I of the spectrum. In addition, the energy domains of the products released (protons and $^{14}C$ nuclei) are larger at high energy, with a double distribution peak for protons at 584 keV and around 0.6 MeV.

The energy histograms of the secondary products resulting from the interaction of high-energy neutrons (part III of the atmospheric spectrum) with the target materials are shown in Figure 14 for $Al_xGa_{1-x}N$ alloys and Figure 15 for diamond and β-$Ga_2O_3$.

Due to the high energy of the incident neutrons in this part of the spectrum, the number of open reaction channels is higher than for neutrons with energies in parts I and II of the neutron spectrum. As a result, in addition to the above-mentioned capture reactions and the elastic and inelastic scattering reactions, other nuclear reactions take place. These additional nuclear reactions produce a wide variety of secondary products that are different from the nuclei of the atoms contained in the materials. Of these additional secondary products, protons and alpha particles are the most numerous; all the others are produced in smaller quantities. For this reason, Figures 14 and 15 show energy histograms for the following products: the nuclei of the atoms contained in the materials, protons, alpha particles, and other products. For the $Al_xGa_{1-x}N$ alloys, Figure 14 shows broad energy distributions for the Ga and N nuclei in GaN (Figure 14a); for Ga, Al and N in $Al_{0.6}Ga_{0.4}N$ (Figure 14b); and for Al and N in AlN (Figure 14c). The maximum value of the distribution is reached at about 0.05 MeV for the Ga nuclei, 0.12 MeV for the Al nuclei, and 0.3 MeV for the N nuclei. The higher the atomic number Z, the lower the energy of the distribution maximum. Likewise, the lighter the nucleus, the higher the energy limit of the nuclei distribution. Protons have a similar distribution, peaking at an energy between 5 and 9 MeV. The distribution is spread over the range 100 keV to 1 GeV for all three materials. Alpha particles have a much narrower distribution and a much lower maximum frequency than any of the other secondary products. A rather broad distribution with a maximum of around 2 MeV is observed for the secondary products grouped under the label 'other' (with atomic numbers other than Z = 1, 2, 7, 13, and 31).

Similar distributions are obtained for diamond and β-$Ga_2O_3$, as shown in Figure 15. Carbon has a very broad energy distribution, peaking around 0.3 MeV and ranging from 10 eV to 20 MeV. Carbon nuclei are the most abundant secondary products over a very wide energy range. In β-$Ga_2O_3$, the Ga and O distributions have maximum frequencies for energies of 0.05 MeV and 0.2 MeV, respectively. As in $Al_xGa_{1-x}N$ alloys, the alpha particles

have a less broad energy distribution, but the maximum frequency is greater in carbon than in all other materials. As mentioned above, alpha particles are the second most abundant secondary products produced in neutron interactions with diamond. Alpha particles are less abundant in all other materials. Finally, the proton distributions in diamond and $\beta$-$Ga_2O_3$ are similar to those of $Al_xGa_{1-x}N$ alloys, with maxima around 10 MeV and a range of energies from tens of keV to 1 GeV. Note that unlike diamond, neutron interactions with $\beta$-$Ga_2O_3$ produce more protons than alpha particles.

## 4. Discussion

The simulation results presented in Section 3 show that AlN is the material that produces the fewest interactions with neutrons over the full neutron spectrum, while GaN is the material that produces the most. For all the materials, more than half of the interactions are the result of interactions with intermediate energy neutrons (part II of the spectrum). In addition, elastic interactions between neutrons and materials account for more than 85% of the total number of interactions. The material producing the fewest secondary products is again AlN, except for neutrons in part I of the spectrum (due to the particular $^{14}N(n,p)^{14}C$ reaction between low-energy neutrons and N, which leads to the production of high-energy protons and $^{14}C$ nuclei). These results give a first indication of the neutron sensitivity of the materials studied here. However, these results also show that a significant amount of the secondary products have very low energies, and thus, they do not deposit enough charge in the materials to disturb the operation of the circuits, as will be explained below. Therefore, the results presented so far need to be refined in order to obtain a more accurate analysis of the response of materials in terms of interactions capable of inducing SEEs in devices and circuits.

The secondary products resulting from the interaction between the neutrons and the material are charged particles that interact with the electrons and nuclei of the target material, causing them to lose energy and slow down. The energy of these charged particles is thus transferred to the material [60] by the ionization mechanism: many excited energetic electrons (delta rays) are produced, electrons that usually have enough energy to ionize other atoms, and a cascade of secondary electrons is generated. These electrons thermalize and create electron–hole pairs along the path of the charged particles [61]. In this way, a large proportion of the energy that is deposited in the semiconductor is converted into electron–hole pairs. The energy required to create an electron–hole pair, $E_{eh}$, is characteristic of each material and depends on the band gap of the material. The values of $E_{eh}$ for the materials studied in this paper are given in Table 1. Following the formation of electron–hole pairs after neutron–matter interactions, the free carriers evolve through several mechanisms. They can recombine with other free carriers, or they can be transported by drift mechanisms in regions exposed to an electric field (e.g., in reverse-biased junctions) or by ambipolar diffusion in the neutral regions of the device [61]. The transported charges can be collected in the junctions and induce a parasitic transient current, which can disturb the normal operation of the device or circuit, thus producing an SEE. The induced disturbances depend on the intensity of the current and the number of circuit nodes affected [47].

Concerning the neutron interactions with UWBG semiconductors studied in this work, the energy distributions of the secondary products presented in Section 3.4 show that a large proportion of these secondaries have very small energies, particularly for interactions with neutrons in parts I and II of the spectrum of atmospheric neutrons. Low-energy products are expected to generate very few electron–hole pairs in the material through the ionization mechanism. Therefore, the amount of charge that these products will deposit in the material will be very small and will not disturb the operation of devices and circuits. For a more accurate analysis and to be able to finely compare the neutron sensitivity of

these materials, it is necessary to consider only those secondary products that are capable of depositing a minimum amount of charge in the material. We set this minimum charge at 0.7 fC, which is the critical charge of a standard 14 nm CMOS SRAM memory cell [62]. To recall, the critical charge for a memory circuit is defined in [63] as the minimum amount of collected charge that causes the logic state of a device node to change, resulting in an SEE. The minimum charge of 0.7 fC corresponds to 4375 electrons, and the energy $E_{min,eh}$ required to create them is obtained for each material as follows:

$$E_{min,eh} = 4375 \times E_{eh} \quad (3)$$

where the energy required to create an electron–hole pair, $E_{eh}$, is given in Table 1. The values of $E_{min,eh}$ for the materials studied here are given in Table 6.

**Table 6.** Minimum energy of the secondary products required to create 4375 electrons, corresponding to a minimum deposited charge of 0.7 fC.

| Semiconductor | GaN | $Al_{0.6}Ga_{0.4}N$ | AlN | Diamond | β-$Ga_2O_3$ |
|---|---|---|---|---|---|
| Minimum energy $E_{min,eh}$ to deposit a charge of 0.7 fC (keV) | 38.9 | 52.9 | 65.6 | 58.6 | 68.2 |

We have therefore eliminated secondary products with energies less than $E_{min,eh}$ from the simulation results for all materials. Figure 16 shows the remaining number of interactions per part of the neutron spectrum, and Table 7 gives the detailed distribution of these interactions according to the reaction mechanism (elastic or inelastic scattering and nuclear reactions) and for each part of the neutron spectrum. Figure 17 shows the total number of these interactions for each material and for the full neutron spectrum with details of the mechanism involved. A comparison of the results in Figure 4 (taking into account all interactions) with those in Figure 16 shows that the elimination of low-energy secondary products results in the removal of a large number of interactions, particularly in parts I and II of the spectrum. Thus, the interactions between low-energy neutrons (part I) and diamond or β-$Ga_2O_3$ are completely excluded (i.e., the secondary products resulting from these interactions do not have the energy necessary to deposit at least 0.7 fC). More specifically, for part I of the spectrum and for all the materials, Table 7 shows that elastic scattering is completely eliminated (there were no inelastic interactions). In this part of the spectrum, only nuclear reactions between neutrons and GaN, $Al_{0.6}Ga_{0.4}N$, or AlN produce secondary products capable of depositing at least 0.7 fC in the material.

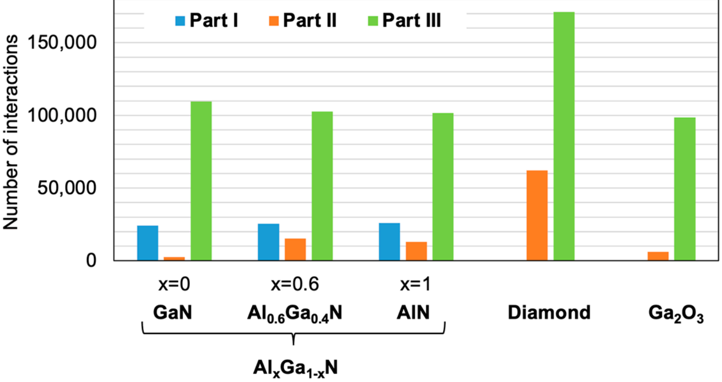


**Figure 16.** Number of interactions capable of depositing at least 0.7 fC of charge in the GaN, $Al_{0.6}Ga_{0.4}N$, diamond, and β-$Ga_2O_3$ bulk targets subjected to part I, part II, and part III of the spectrum of atmospheric neutrons (Figure 2) for an equivalent exposure time of $2.5 \times 10^7$ h.

**Table 7.** Number of events of elastic and inelastic scattering and nuclear reactions capable of depositing at least 0.7 fC of charge in the GaN, $Al_{0.6}Ga_{0.4}N$, diamond, and β-$Ga_2O_3$ bulk targets subjected to part I, part II, and part III of the spectrum of atmospheric neutrons (Figure 2) for an equivalent exposure time of 2.5 × $10^7$ h.

| Part of the Neutron Spectrum | Material | Elastic | Inelastic | Nuclear |
|---|---|---|---|---|
| Part I | GaN | 0 | 0 | 24,328 |
| | $Al_{0.6}Ga_{0.4}N$ | 0 | 0 | 24,498 |
| | AlN | 0 | 0 | 26,081 |
| | Diamond | 0 | 0 | 0 |
| | β-$Ga_2O_3$ | 0 | 0 | 0 |
| Part II | GaN | 0 | 0 | 2466 |
| | $Al_{0.6}Ga_{0.4}N$ | 14,045 | 0 | 1241 |
| | AlN | 11,868 | 0 | 1254 |
| | Diamond | 62,148 | 0 | 0 |
| | β-$Ga_2O_3$ | 6150 | 0 | 0 |
| Part III | GaN | 54,687 | 18,844 | 35,884 |
| | $Al_{0.6}Ga_{0.4}N$ | 58,693 | 13,797 | 30,101 |
| | AlN | 62,901 | 11,777 | 26,884 |
| | Diamond | 133,399 | 9124 | 28,641 |
| | β-$Ga_2O_3$ | 52,880 | 11,863 | 33,917 |

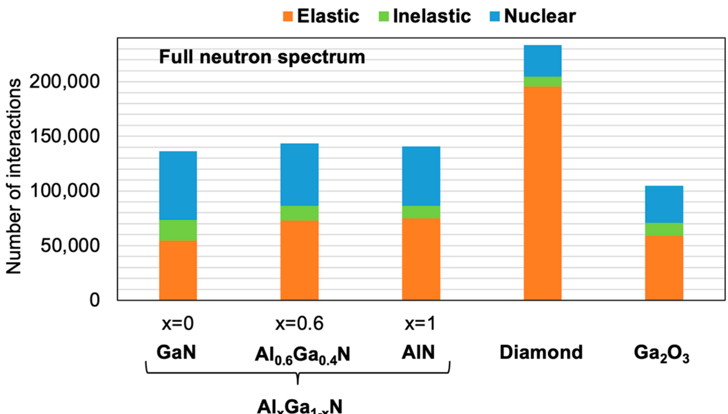


**Figure 17.** Total number of interactions capable of depositing at least 0.7 fC of charge in the GaN, $Al_{0.6}Ga_{0.4}N$, diamond, and β-$Ga_2O_3$ bulk targets under the full spectrum of atmospheric neutron shown in Figure 2 for an equivalent exposure time of 2.5 × $10^7$ h.

Regarding the interactions with neutrons in part II of the spectrum (intermediate energy), many of these interactions are eliminated, especially for GaN and β-$Ga_2O_3$. In this part, inelastic interactions are eliminated for all the materials. In addition, for GaN, only some of the nuclear reactions produce products of sufficient energy (the elastic reactions are eliminated). For the other materials, only recoils from some of the elastic interactions remain, as well as a small number of nuclear reactions for $Al_{0.6}Ga_{0.4}N$ and AlN. In contrast to parts I and II, the number of interactions with neutrons that give secondary products capable of depositing at least 0.7 fC is much higher in part III. This result was expected, since the high-energy neutrons involved in these interactions transfer a significant part of their energy to the secondary products. These products will therefore have higher energies than those resulting from interactions with low- and intermediate-energy neutrons.

The results in Figures 16 and 17 directly compare the atmospheric neutron response of UWBG semiconductors from the point of view of the number of interactions that can trigger SEEs in a device or circuit. Figure 17 shows that diamond is the most sensitive material to neutrons in the whole spectrum, principally because of the very large number of elastic interactions (especially in parts II and III, see Table 7), while β-$Ga_2O_3$ is the least sensitive material, with more than half as many interactions as diamond. $Al_xGa_{1-x}N$ alloys are less sensitive than diamond, with about 40% fewer interactions and more than half the number

of elastic interactions. Figure 16 shows that diamond and β-$Ga_2O_3$ are not sensitive to low-energy neutrons, whereas $Al_xGa_{1-x}N$ alloys are sensitive to thermal neutrons due to the presence of N, which interacts with these neutrons in the $^{14}N(n,p)^{14}C$ reaction and produces high-energy protons and $^{14}C$ nuclei, as explained in Section 3. These results at the material level have important implications for electronic devices and circuits in terms of technological choices. Thus, for applications in which neutrons with thermal or low energies are a significant concern, diamond- or β-$Ga_2O_3$-based electronic devices should be preferred over $Al_xGa_{1-x}N$ alloy-based devices. Furthermore, for such applications, $Al_xGa_{1-x}N$ alloy-based devices and circuits should be used with particular caution, for example, by using absorbing materials such as $B_4C$ to eliminate thermal neutrons. For medium- and high-energy neutrons, Figure 16 shows that diamond is much more sensitive than the other materials. For high-energy neutrons, the number of interactions with diamond is almost twice that of the other materials, while $Al_xGa_{1-x}N$ alloys and β-$Ga_2O_3$ have equivalent sensitivity. Therefore, these results indicate that for applications involving high-energy neutrons, electronic devices based on $Al_xGa_{1-x}N$ alloys or β-$Ga_2O_3$ should be preferred over those based on diamond.

## 5. Conclusions

In this study, we conducted an extensive simulation analysis of the interactions between atmospheric neutrons and UWBG semiconductors, specifically focusing on $Al_xGa_{1-x}N$ alloys, diamond, and β-$Ga_2O_3$. Our results indicate significant variations in single-particle neutron sensitivity among these materials, driven primarily by differences in their atomic compositions and interaction mechanisms. The study reveals that a very large proportion of the secondary products of these interactions are low energy, producing very small amounts of electron–hole pairs that are unlikely to produce SEEs. Thus, a detailed analysis has been carried out by considering only those interactions that are able to deposit a charge of at least 0.7 fC (the critical charge of a standard 14 nm CMOS SRAM memory cell) in the device. The results of this analysis show that diamond exhibits the highest sensitivity across the entire neutron spectrum, primarily due to its high elastic scattering cross-section, while β-$Ga_2O_3$ emerges as the least sensitive material, with more than half as many interactions as diamond. The analysis further highlights that $Al_xGa_{1-x}N$ alloys exhibit a moderate neutron sensitivity, with a number of interactions that is approximately the same for all $Al_xGa_{1-x}N$ alloys. Furthermore, the interactions with neutrons that produce secondary products capable of depositing significant charge are more prevalent for high-energy neutrons (part III of the atmospheric neutron spectrum). Our results also suggest that for electronic applications where exposure to thermal or low-energy neutrons is critical, diamond and β-$Ga_2O_3$ should be preferred over $Al_xGa_{1-x}N$ alloys. However, $Al_xGa_{1-x}N$ and β-$Ga_2O_3$ appear to be more resilient choices than diamond when considering high-energy neutron environments. These simulation results offer valuable insights for the design of radiation-tolerant electronic components and may guide the selection of materials based on specific operational environments. Future work should focus on experimental validation of these simulation results, including device-level assessments, to fully understand the impact of single-particle neutron interactions on circuit performance and reliability. In addition, exploration of neutron shielding techniques, such as the integration of boron-based materials, could further enhance the radiation hardness of $Al_xGa_{1-x}N$-based devices in critical applications.

**Author Contributions:** Conceptualization, D.M. and J.-L.A.; methodology, D.M. and J.-L.A.; software, D.M. and J.-L.A.; formal analysis, D.M. and J.-L.A.; investigation, D.M. and J.-L.A.; writing—review and editing, D.M. and J.-L.A.; visualization, D.M. and J.-L.A. All authors have read and agreed to the published version of the manuscript.

**Funding:** This research received no external funding.

**Data Availability Statement:** The original contributions presented in this study are included in the article. Further inquiries can be directed to the corresponding author.

**Acknowledgments:** The authors would like to sincerely thank Paul Goldhagen (U.S. Department of Homeland Security) for permission to use the experimental neutron spectrum data.

**Conflicts of Interest:** The authors declare no conflicts of interest.

## References

1. Wong, M.H.; Bierwagen, O.; Kaplar, R.J.; Umezawa, H. Ultrawide-bandgap semiconductors: An overview. *J. Mater. Res.* **2021**, *36*, 4601–4615. [CrossRef]
2. Tsao, J.Y.; Chowdhury, S.; Hollis, M.A.; Jena, D.; Johnson, N.M.; Jones, K.A.; Kaplar, R.J.; Rajan, S.; Van de Walle, C.G.; Bellotti, E.; et al. Ultrawide-Bandgap Semiconductors: Research Opportunities and Challenges. *Adv. Electron. Mater.* **2018**, *4*, 1600501. [CrossRef]
3. Yang, J.; Liu, K.; Chen, X.; Shen, D. Recent advances in optoelectronic and microelectronic devices based on ultrawide-bandgap semiconductors. *Prog. Quantum Electron.* **2022**, *83*, 100397. [CrossRef]
4. Slobodyan, O.; Flicker, J.; Dickerson, J.; Shoemaker, J.; Binder, A.; Smith, T.; Goodnick, S.; Kaplar, R.; Hollis, M. Analysis of the dependence of critical electric field on semiconductor bandgap. *J. Mater. Res.* **2021**, *37*, 849–865. [CrossRef]
5. Chow, T.P.; Tyagi, R. Wide bandgap compound semiconductors for superior high-voltage unipolar power devices. *IEEE Trans. Electron Devices* **1994**, *41*, 1481–1483. [CrossRef]
6. Umezawa, H. Recent advances in diamond power semiconductor devices. *Mater. Sci. Semicond. Process.* **2018**, *78*, 147. [CrossRef]
7. Wong, M.H.; Higashiwaki, M. Vertical β-$Ga_2O_3$ power transistors: A review. *IEEE Trans. Electron Devices* **2020**, *67*, 3925–3937. [CrossRef]
8. Qiao, R.; Zhang, H.; Zhao, S.; Yuan, L.; Jia, R.; Peng, B.; Zhang, Y. A state-of-art review on gallium oxide field-effect transistors. *J. Phys. D Appl. Phys.* **2022**, *55*, 383003. [CrossRef]
9. Zhang, M.; Liu, Z.; Yang, L.; Yao, J.; Chen, J.; Zhang, J.; Wei, W.; Guo, Y.; Tang, W. β-$Ga_2O_3$-Based Power Devices: A Concise Review. *Crystals* **2022**, *12*, 406. [CrossRef]
10. Xue, H.; He, Q.; Jian, G.; Long, S.; Pang, T.; Liu, M. An Overview of the Ultrawide Bandgap $Ga_2O_3$ Semiconductor-Based Schottky Barrier Diode for Power Electronics Application. *Nanoscale Res. Lett.* **2018**, *13*, 290. [CrossRef]
11. He, J. Comparison between the ultra-wide band gap semiconductor AlGaN and GaN. *IOP Conf. Ser. Mater. Sci. Eng.* **2020**, *738*, 012009. [CrossRef]
12. Baca, A.G.; Armstrong, A.M.; Allerman, A.A.; Douglas, E.A.; Sanchez, C.A.; King, M.P.; Coltrin, M.E.; Fortune, T.R.; Kaplar, R.J. An AlN/$Al_{0.85}Ga_{0.15}N$ high electron mobility transistor. *Appl. Phys. Lett.* **2016**, *109*, 033509. [CrossRef]
13. Isberg, J.; Hammersberg, J.; Johansson, E.; Wikström, T.; Twitchen, D.J.; Whitehead, A.J.; Coe, S.E.; Scarsbrook, G.A. High carrier mobility in single-crystal plasma-deposited diamond. *Science* **2002**, *297*, 1670. [CrossRef] [PubMed]
14. Xue, H.; Lee, C.H.; Hussian, K.; Razzak, T.; Abdullah, M.; Xia, Z.; Sohel, S.H.; Khan, A.; Rajan, S.; Lu, W. $Al_{0.75}Ga_{0.25}N$/$Al_{0.60}Ga_{0.40}N$ heterojunction field effect transistor with fT of 40 GHz. *Appl. Phys. Express* **2019**, *12*, 066502. [CrossRef]
15. Armstrong, A.M.; Klein, B.; Allerman, A.A.; Douglas, E.A.; Baca, A.G.; Crawford, M.H.; Pickrell, G.W.; Sanchez, C.A. Visible-blind and solar-blind detection induced by defects in AlGaN high electron mobility transistors. *J. Appl. Phys.* **2018**, *123*, 114502. [CrossRef]
16. Jiang, H.X.; Lin, J.Y. AlGaN and InAlGaN alloys-epitaxial growth, optical and electrical properties, and applications. *Opto-Electron. Rev.* **2002**, *10*, 271–286.
17. Xu, M.; Wang, D.; Fu, K.; Mudiyanselage, H.D.; Fu, H.; Zhao, Y. A review of ultrawide bandgap materials: Properties, synthesis and devices. *Oxf. Open Mater. Sci.* **2022**, *2*, itac004. [CrossRef]
18. He, H.; Zhao, J.; Byggmästar, J.; He, R.; Nordlund, K.; He, C.; Djurabekova, F. Threshold displacement energy map of Frenkel pair generation in β-$Ga_2O_3$ from machine-learning-driven molecular dynamics simulations. *Acta Mater.* **2024**, *276*, 120087. [CrossRef]
19. Pearton, S.; Aitkaliyeva, A.; Xian, M.; Ren, F.; Khachatrian, A.; Ildefonsorosa, A.; Islam, Z.; Rasel, M.; Haque, A.; Polyakov, A.; et al. Review—Radiation Damage in Wide and Ultra-Wide Bandgap Semiconductors. *ECS J. Solid State Sci. Technol.* **2021**, *10*, 055008. [CrossRef]

20. Yu, C.; Guo, H.; Liu, Y.; Wu, X.; Zhang, L.; Tan, X.; Han, Y.; Ren, L. Simulation study on single-event burnout in field-plated $Ga_2O_3$ MOSFETs. *Microelectron. Reliabil.* **2023**, *149*, 115227. [CrossRef]
21. Zhang, J.; Dong, P.; Dang, K.; Zhang, Y.; Yan, Q.; Xiang, H.; Su, J.; Liu, Z.; Si, M.; Gao, J.; et al. Ultra-wide bandgap semiconductor $Ga_2O_3$ power diodes. *Nat. Commun.* **2022**, *13*, 3900. [CrossRef] [PubMed]
22. Gao, H.; Ahsanullah, D.; Baumann, R.; Gnade, B. A Study of Neutron Induced Single-Event Damage in AlGaN/GaN HEMTs. In Proceedings of the 2022 IEEE Radiation Effects Data Workshop (REDW), Provo, UT, USA, 12–18 July 2022; pp. 1–6.
23. Munteanu, D.; Autran, J.-L. Basic Mechanisms of Single-Event Occurrence in Silicon Carbide Semiconductor under Terrestrial Atmospheric Neutron Irradiation. *Electronics* **2023**, *12*, 4468. [CrossRef]
24. Leray, J.L. Effects of atmospheric neutrons on devices, at sea level and in avionics embedded systems. *Microelectron. Reliabil.* **2007**, *47*, 1827–1835. [CrossRef]
25. Chabak, K.D.; Leedy, K.D.; Green, A.J.; Mou, S.; Neal, A.T.; Asel, T.; Heller, E.R.; Hendricks, N.S.; Liddy, K.; Crespo, A.; et al. Lateral $\beta$-$Ga_2O_3$ field effect transistors. *Semicond. Sci. Technol.* **2020**, *35*, 013002. [CrossRef]
26. Muhtadi, S.; Hwang, S.M.; Coleman, A.; Asif, F.; Simin, G.; Chandrashekhar, M.V.S.; Khan, A. High electron mobility transistors with $Al_{0.65}Ga_{0.35}N$ channel layers on thick AlN/sapphire templates. *IEEE Electron Device Lett.* **2017**, *38*, 914–917. [CrossRef]
27. Allerman, A.A.; Armstrong, A.M.; Fischer, A.J.; Dickerson, J.R.; Crawford, M.H.; King, M.P.; Moseley, M.W.; Wierer, J.J.; Kaplar, R.J. $Al_{0.3}Ga_{0.7}N$ PN diode with breakdown Voltage >1600 V. *Electron. Lett.* **2016**, *52*, 1319–1321. [CrossRef]
28. Xie, J.; Mia, S.; Dalmau, R.; Collazo, R.; Rice, A.; Tweedie, J.; Sitar, Z. Ni/Au Schottky diodes on $Al_xGa_{1-x}N$ ($0.7<x<1$) grown on AlN single crystal substrates. *Phys. Status Solidi C* **2011**, *8*, 2407–2409.
29. Iwasaki, T.; Yaita, J.; Kato, H.; Makino, T.; Ogura, M.; Takeuchi, D.; Okushi, H.; Yamasaki, S.; Hatano, M. 600 V diamond junction field-effect transistors operated at 200 °C. *IEEE Electron Device Lett.* **2014**, *35*, 241–243. [CrossRef]
30. Masante, C.; Rouger, N.; Pernot, J. Recent progresses in deep-depletion diamond metal–oxide–semiconductor field-effect transistors. *J. Phys. D Appl. Phys.* **2021**, *54*, 233002. [CrossRef]
31. Munteanu, D.; Autran, J.L. Susceptibility of Group-IV and III-V Semiconductor-based Electronics to Atmospheric Neutrons Explored by Geant4 Numerical Simulations. In *Numerical Simulations*; Rao, S., Ed.; IntechOpen: London, UK, 2018; pp. 117–134.
32. Autran, J.-L.; Munteanu, D. Comparative Radiation Response of GaN and $Ga_2O_3$ Exposed to Ground-Level Neutrons. *Crystals* **2024**, *14*, 128. [CrossRef]
33. Autran, J.L.; Munteanu, D. Radiation Response of Group-IV and III-V Semiconductors Subjected to D–D and D–T Fusion Neutrons. In *New Advances in Semiconductors*; Cavalheiro, A.A., Ed.; IntechOpen: London, UK, 2022; pp. 1–21.
34. Agostinelli, S.; Allison, J.; Amako, K.; Apostolakis, J.; Araujo, H.; Arce, P.; Asai, M.; Axen, D.; Banerjee, S.; Barrand, G.; et al. Geant4—A simulation toolkit. *Nucl. Instrum. Meth. A* **2003**, *506*, 250–303. [CrossRef]
35. Allison, J.; Amako, K.; Apostolakis, J.; Araujo, H.; Arce Dubois, P.; Asai, M.; Barrand, G.; Capra, R.; Chauvie, S.; Chytraceket, R.; et al. Geant4 developments and applications. *IEEE Trans. Nucl. Sci.* **2006**, *53*, 270–278. [CrossRef]
36. Allison, J.; Amako, K.; Apostolakis, J.; Arce, P.; Asai, M.; Aso, T.; Bagli, E.; Bagulya, A.; Banerjee, S.; Barrand, G.; et al. Recent developments in Geant4. *Nucl. Instrum. Meth. A* **2016**, *835*, 186–225. [CrossRef]
37. Adachi, S. III-V Ternary and Quaternary Compounds. In *Springer Handbook of Electronic and Photonic Materials*; Kasap, S., Capper, P., Eds.; Springer International Publishing AG: Cham, Switzerland, 2017; pp. 725–741.
38. Coffie, R.L. High Power High Frequency Transistors: A Material's Perspective. In *High-Frequency GaN Electronic Devices*; Fay, P., Jena, D., Maki, P., Eds.; Springer International Publishing: Cham, Switzerland, 2020; pp. 5–41.
39. Yakimov, E.B.; Polyakov, A.Y.; Shchemerov, I.V.; Smirnov, N.B.; Vasilev, A.A.; Vergeles, P.S.; Yakimov, E.E.; Chernykh, A.V.; Ren, F.; Pearton, S.J. Experimental estimation of electron–hole pair creation energy in $\beta$-$Ga_2O_3$. *Appl. Phys. Lett.* **2021**, *118*, 202106. [CrossRef]
40. Zoroddu, A.; Bernardini, F.; Ruggerone, P.; Fiorentini, V. First-principles prediction of structure, energetics, formation enthalpy, elastic constants, polarization, and piezoelectric constants of AlN, GaN, and InN: Comparison of local and gradient- corrected density-functional theory. *Phys. Rev. B* **2001**, *64*, 045208. [CrossRef]
41. Phillips, J.C. *Bonds and Bands in Semiconductors*; Academic Press: New York, NY, USA, 1973.
42. Koide, Y.; Itoh, H.; Khan, M.R.H.; Hiramatu, K.; Sawaki, N.; Akasaki, I. Energy band-gap bowing parameter in an $Al_xGa_{1-x}N$ alloy. *J. Appl. Phys.* **1987**, *61*, 4540–4543. [CrossRef]
43. Ferreyra, R.A.; Zhu, C.; Teke, A.; Morkoç, H. Group III Nitride. In *Springer Handbook of Electronic and Photonic Materials*; Kasap, S., Capper, P., Eds.; Springer International Publishing AG: Cham, Switzerland, 2017; pp. 743–827.
44. Dridi, Z.; Bouhafs, B.; Ruterana, P. First-principles investigation of lattice constants and bowing parameters in wurtzite $Al_xGa_{1-x}N$, $In_xGa_{1-x}N$ and $In_xAl_{1-x}N$ alloys. *Semicond. Sci. Technol.* **2003**, *18*, 850–856. [CrossRef]
45. Yun, F.; Reshchikov, M.A.; He, L.; King, T.; Morkoç, H.; Novak, S.W.; Wei, L. Energy band bowing parameter in Alx Ga1-x N alloys. *J. Appl. Phys.* **2002**, *92*, 4837. [CrossRef]
46. Klein, C.A. Bandgap Dependence and Related Features of Radiation Ionization Energies in Semiconductors. *J. Appl. Phys.* **1968**, *39*, 2029–2038. [CrossRef]

47. Autran, J.L.; Munteanu, D. *Soft Errors: From Particles to Circuits*; Taylor & Francis/CRC Press: Boca Raton, FL, USA, 2015.
48. Gordon, M.S.; Goldhagen, P.; Rodbell, K.P.; Zabel, T.H.; Tang, H.H.K.; Clem, J.M.; Bailey, P. Measurement of the Flux and Energy Spectrum of Cosmic-Ray Induced Neutrons on the Ground. *IEEE Trans. Nucl. Sci.* **2004**, *51*, 3427–3434. [CrossRef]
49. Goldhagen, P. Cosmic-Ray Neutrons on the Ground and in the Atmosphere. *MRS Bull.* **2003**, *28*, 131–135. [CrossRef]
50. Rinard, P. Neutron Interactions with Matter. Los Alamos Technical Report, 1991. Available online: https://www.gammaexplorer.com/lanlreports/lanl1_a/lib-www/la-pubs/00326407.pdf (accessed on 15 January 2025).
51. Autran, J.L.; Munteanu, D. Atmospheric Neutron Radiation Response of III-V Binary Compound Semiconductors. *IEEE Trans. Nucl. Sci.* **2020**, *67*, 1428–1435. [CrossRef]
52. TENDL-2021. TALYS-Based Evaluated Nuclear Data Library. Available online: https://tendl.web.psi.ch/tendl_2021/tendl2021.html (accessed on 8 November 2024).
53. Serre, S.; Semikh, S.; Uznanski, S.; Autran, J.L.; Munteanu, D.; Gasiot, G.; Roche, P. Geant4 Analysis of n-Si Nuclear Reactions From Different Sources of Neutrons and Its Implication on Soft-Error Rate. *IEEE Trans. Nucl. Sci.* **2012**, *59*, 714–722. [CrossRef]
54. Geant4 General Particle Source (GPS). Available online: https://www.fe.infn.it/u/paterno/Geant4_tutorial/slides_further/GPS/GPS_manual.pdf (accessed on 20 November 2024).
55. Geant4 Version 4.9.4. Available online: http://geant4.in2p3.fr/IMG/pdf_PhysicsLists.pdf (accessed on 20 November 2024).
56. Munteanu, D.; Autran, J.L. Modeling and Simulation of Single-Event Effects in Digital Devices and ICs. *IEEE Trans. Nucl. Sci.* **2008**, *55*, 1854–1878. [CrossRef]
57. Baker, D.E. Graphite as a neutron moderator and reflector material. *Nucl. Eng. Des.* **1971**, *14*, 413–444. [CrossRef]
58. Gaillard, R. Single Event Effects: Mechanisms and Classification. In *Soft Errors in Modern Electronic Systems*; Nicolaidis, M., Ed.; Springer: New York, NY, USA, 2011.
59. Coronetti, A.; Alía, R.G.; Lucsanyi, D.; Letiche, M.; Kastriotou, K.; Cazzaniga, C.; Frost, C.D.; Saigné, F. An Analysis of the Significance of the $^{14}N(n,p)^{14}C$ Reaction for Single-Event Upsets Induced by Thermal Neutrons in SRAMs. *IEEE Trans. Nucl. Sci.* **2023**, *70*, 1634–1642. [CrossRef]
60. Leroy, C.; Rancoita, P.G. *Principes of Radiation Interaction Matter and Detection*; World Scientific Publishing: Singapore, Singapore, 2004.
61. Autran, J.L.; Munteanu, D. Multiscale, Multiphysics Modeling and Simulation of Single-Event Effects in Digital Electronics: From Particles to Systems. *IEEE Trans. Nucl. Sci.* **2024**, *71*, 31–66. [CrossRef]
62. Seifert, N.; Jahinuzzaman, S.; Velamala, J.; Ascazubi, R.; Patel, N.; Gill, B.; Basile, J.; Hicks, J. Soft Error Rate Improvements in 14-nm Technology Featuring Second-Generation 3D Tri-Gate Transistors. *IEEE Trans. Nucl. Sci.* **2012**, *62*, 2570–2577. [CrossRef]
63. *JESD89B*; Measurement and Reporting of Alpha Particle and Terrestrial Cosmic Ray-Induced Soft Errors in Semiconductor Devices; Revision of JESD89A. JEDEC: Arlington, VA, USA, 2021.

**Disclaimer/Publisher's Note:** The statements, opinions and data contained in all publications are solely those of the individual author(s) and contributor(s) and not of MDPI and/or the editor(s). MDPI and/or the editor(s) disclaim responsibility for any injury to people or property resulting from any ideas, methods, instructions or products referred to in the content.